

Land Surfaces at the Tipping-Point for Water and Energy Balance Coupling

Jianzhi Dong^{1,2}, Ruzbeh Akbar², Andrew F. Feldman^{3,4}, Daniel Short Gianotti², Dara Entekhabi²

1. Institute of Surface-Earth System Science, Tianjin University, Tianjin, China

2. Department of Civil and Environmental Engineering, MIT, Cambridge, Massachusetts 02139, USA

3. Biospheric Sciences Laboratory, NASA Goddard Space Flight Center, Greenbelt, Maryland, USA

4. NASA Postdoctoral Program, NASA Goddard Space Flight Center, Greenbelt, Maryland, USA

Abstract

The surface water and energy balances can be coupled or uncoupled depending on whether the evaporation regime is water-limited or energy-limited. As the landscape loses soil moisture during drydowns, a transition between the regimes may occur, which signifies a nonlinear change in water-energy-carbon coupling. Regions that switch often between these two regimes, i.e., are dominated by neither regime, are particularly vulnerable to climate variability and change. To robustly identify these tipping points, we identify drydown events based on global soil moisture data sets from remote sensing. The event identification does not rely on precipitation information and is robust with respect to measurement noise. Then, the soil moisture thresholds delineating the evaporation regime transitions are determined by Sequential Monte Carlo Sampling and a two-stage parametrization strategy. Based on the estimated soil moisture thresholds across the globe, we estimate observation-based water availability indices which quantify the nonlinear controls of soil moisture on evaporation. This framework is tested and applied globally using Soil Moisture Active Passive (SMAP) soil moisture retrievals. Combined with a new tipping-point metric that describes the frequency of evaporation regime transitions, we identify regions that switch often between different evaporation regimes at the global scale. Given unit shifts in soil moisture, these regions will experience the most change in how their surface water and energy are coupled.

1. Introduction

Evaporation flux couples the water, energy and carbon balances over land surfaces (Biederman et al. 2018; Crow et al. 2019; Entekhabi et al. 1996; Santanello Jr et al. 2019). During drydowns and depending on the availability of volumetric soil moisture (θ), microclimate

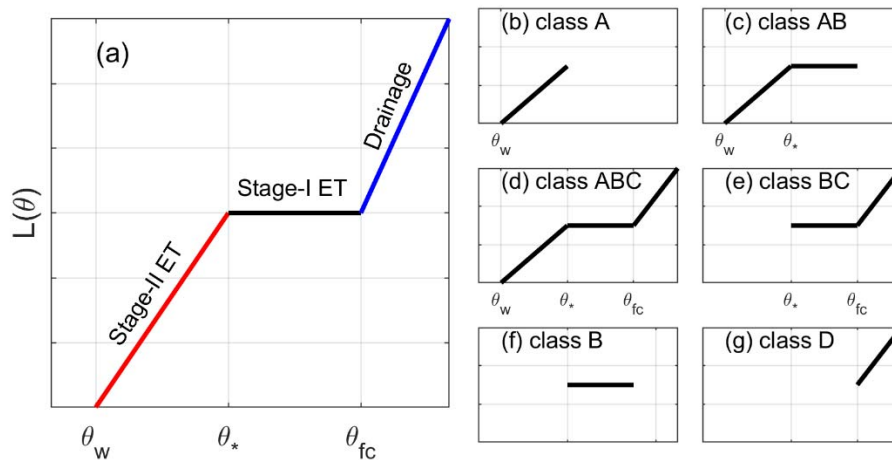
30 and landscape attributes, evaporation can be classified to be in energy- (Stage-I) or
31 water-limited (Stage-II) regimes (Gallego-Elvira et al. 2016; Greve et al. 2015; Seneviratne et al.
32 2010).

33 Transitions between Stage-I and II evaporation regimes determine the degree of coupling
34 between the water, energy and carbon fluxes and states (Feldman et al. 2019, 2020; Miralles et
35 al. 2019). Specifically, soil moisture's control on evaporation abruptly increases once it drops
36 below a critical value θ_* (denotes the onset of Stage-II evaporation), which will subsequently
37 elevate local air temperature via land-atmosphere coupling (Orth 2021). For some extreme
38 cases, this mechanism can increase air temperature to soil moisture sensitivity by four times –
39 leading to exacerbated local heatwaves (Dirmeyer et al. 2021). Likewise, such mechanisms are
40 also often responsible for local drought intensification and global carbon uptake variability
41 (Humphrey et al. 2021; Seneviratne et al. 2010; Zhou et al. 2019). Therefore, landscapes with
42 frequent evaporation regime transitions (or land surface tipping-points) are more sensitive to
43 climate change/variability, since dry anomalies can be amplified via land-atmosphere coupling
44 (Schwingshackl et al. 2017).

45 However, existing physical models contain substantial uncertainties in capturing the
46 tipping-point locations and the associated regime change frequencies (Schwingshackl et al.
47 2017). This is because model representations of soil moisture's control on evaporation are
48 highly uncertain (Crow et al. 2015; Dirmeyer et al. 2000; Lorenz et al. 2016). For example, Dong
49 et al. (2020b) demonstrates that most land surface model schemes preferentially classify the
50 central US into water-limited evaporation regimes, leading to overestimated evaporation water
51 stress and biases in screen-level air temperature estimates (Crow et al. 2020). Likewise,
52 modeled evaporation and soil moisture correlations (higher for water-limited dominated
53 evaporation regimes) are typically biasedly higher than that of observations (Crow et al. 2015;
54 Dirmeyer et al. 2018; Dong et al. 2022b; Lei et al. 2018), which may be a key source of projected
55 air temperature uncertainty in atmospheric models (Berg and Sheffield 2018; Dong et al. 2022b;
56 Seneviratne et al. 2013). Therefore, observed land tipping-point distributions and the associated
57 evaporation changes are of paramount importance for improving and diagnosing large-scale
58 modeling frameworks.

59 Although evaporation regimes and land tipping points can be identified using observed
60 evaporation and soil moisture data pairs (Buitink et al. 2020; Dirmeyer et al. 2018; Williams and

61 Torn 2015), flux tower based evaporation observations have limited spatial availability (Holmes
 62 et al. 2018). Remotely sensed evaporation has been used for diagnosing large-scale soil
 63 moisture – evaporation relationships and the associated critical soil moisture thresholds
 64 (Denissen et al. 2020; Hain et al. 2009; Miralles et al. 2012). However, algorithmic and retrieval
 65 uncertainties in these evaporation estimates can mask soil moisture and evaporation
 66 relationships (Crow et al. 2015; Lei et al. 2018). More importantly, remote sensing based
 67 evaporation products may involve pre-defined evaporation and soil moisture relationships
 68 (Martens et al. 2017) – making them difficult to be used as an objective reference (Qiu et al.
 69 2020). Evaporation regimes can also be identified using the diurnal amplitude of land surface
 70 temperature and air temperature changing rates (Feldman et al. 2020; Gallego-Elvira et al.
 71 2016). However, the evaporation and land surface temperature relationship is complicated by a
 72 multitude of factors (Bateni et al. 2014; Lu et al. 2016).



73

74 **Figure 1.** Key hydrological regimes dominating soil moisture losses during interstorm periods (a).
 75 The black, red and blue solid lines represent stage-I and II evaporation and drainage hydrological
 76 regimes, respectively. The presence of different hydrological regimes is driven by microclimate
 77 and landscape attributes, and the potential combinations of hydrological regimes are shown in
 78 parts b to g – representing soil loss function $L(\theta)$ shapes vary from dry to wet conditions. θ_w ,
 79 θ_* and θ_{fc} represent the wilting point, critical evaporation regime transition point and field
 80 capacity, respectively, which are used for characterizing $L(\theta)$.

81 Alternatively, the large scale signature of different evaporation regimes can be identified
 82 using remote sensing soil moisture interstorm drydown patterns, without evaporation
 83 observations or proxies (Akbar et al. 2018; Sehgal et al. 2021b). Specifically, on
 84 non-precipitation days, soil moisture loss (i.e., the rate of soil moisture temporal change during

85 drydowns) is dominated by water- and energy-limited evaporation and drainage regimes. The
86 transition of different evaporation regimes can be identified when soil moisture crosses the
87 critical value θ_* – see Figure 1 (Akbar et al. 2018). However, such methods typically require
88 high-quality precipitation data or (arbitrarily) defined thresholds to identify soil moisture
89 drydown time series. Additionally, numerous free parameters need to be optimized from a
90 single soil moisture drydown time series, which undermines the robustness of the results.

91 This study seeks to further advance large-scale soil moisture drydown analysis, and we aim
92 to provide observation-based identification of tipping-points that represent landscapes with
93 frequent switches between different evaporation regimes. To do so, we first present an
94 improved soil moisture drydown identification and parameterization framework. Then, an
95 observation-based measure of land evaporation water availability index (Π) is introduced and
96 evaluated using flux tower observations. Based on Π , we further propose a new tipping-point
97 metric (Φ), which quantifies the frequency of a landscape switching between water- and
98 energy-limited evaporation regimes. Our main result is the observation-based identification of
99 surface water, energy and carbon balance tipping-points, which identify regions likely to be
100 more vulnerable to climate variability and change.

101 2. Methods and Data

102 The shifts in evaporation regimes occur during interstorm periods where soil moisture is
103 persistently decreasing. To determine the critical soil moisture value θ_* that marks the
104 evaporation regime change, interstorm soil moisture drydown periods need to be isolated first.
105 Therefore, a robust interstorm drydown identification method is first presented in Section 2.1.

106 After the isolation of drydowns, five parameters (three soil moisture thresholds and two loss
107 rates, Figure 1a) need to be determined. Based on Sequential Monte Carlo Sampling (SMCS;
108 Jeremiah et al. 2012)), we propose a two-stage optimization framework in Section 2.2. This
109 framework can robustly determine $L(\theta)$ forms and the associated parameters – see Section 1
110 of the Supporting Information.

111 Combined with metrics proposed in Section 2.3, the soil moisture drydown analysis is used
112 to quantify global evaporation water availability and land surface tipping points. All the data
113 used in our analysis is described in Section 2.4.

114

115 2.1 Soil moisture drydown identification

116 Surface volumetric soil moisture content (θ) temporal dynamics during interstorms are
117 dissipative and exhibit a Markovian behavior (Crow et al. 2009; Dong and Crow 2018; Short
118 Gianotti et al. 2019b) so that during the entire time-series:

$$\theta_t = \lambda^\tau \theta_{t-\tau} + \zeta_t \quad (1)$$

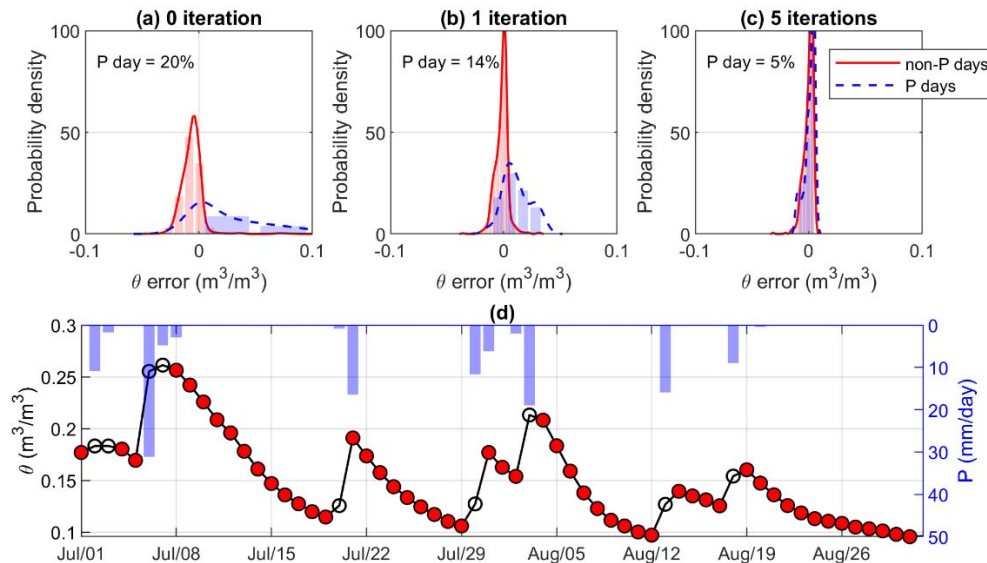
$$\zeta_t = I_t + \epsilon_t \quad (2)$$

119 where τ denotes the temporal difference of two consecutive soil moisture observations in
120 days (overpasses); $I_t \geq 0$ is infiltration due to precipitation addition (zero for non-precipitation
121 days); λ is a dimensionless temporal constant describing the θ decorrelation at daily time
122 scales; ϵ_t is zero-mean random error.

123 According to (1), ζ_t represents the error of approximating θ_t with $\lambda^\tau \theta_{t-\tau}$, which is a
124 combination of random errors (in non-precipitation days) and positive outliers (i.e., $I_t > 0$, in
125 precipitation days) – see Figure 2a for demonstration. Days in which θ is strongly affected by
126 I_t can be identified as positive outliers of ζ_t , which can be iteratively removed.

127 An illustrative example of this drydown identification procedure based on in-situ soil
128 moisture observations from Oklahoma is shown in Figure 2, in which 20% of days experience
129 precipitation. To start, we directly fit the observed θ time series as $\lambda^\tau \theta_{t-\tau}$, which yields
130 contrasting errors (ζ_t) in precipitation and non-precipitation days (see the blue and red
131 histograms in Figure 2a). Assuming the error ζ_t is zero-mean and normally distributed and
132 based on its standard deviation, we can identify (via one-sample t-test) and filter out days that
133 ζ_t realizations are outliers to the expected distribution. By repeating the above procedure, θ
134 observations that are significantly affected by precipitation are iteratively removed and only
135 drydowns remain (Figure 2b, c and d). The approach is tested and is reasonably robust to the
136 choice of confidence level for identifying the positive ζ_t outliers. Higher t-test confidence
137 levels require more iterations to converge on the appropriate drydown identification. In this
138 study, we use a confidence level of $p = 0.90$, which yields clear $d\theta/dt$ vs. θ relationships with

139 efficient algorithmic convergence.



140

141 **Figure 2.** The distribution of θ estimation error (ζ_t) using $\theta_t = \lambda^\tau \theta_{t-\tau}$ for different iterations
142 of outlier removal (a to c), with text denoting the observed portion of precipitation days in the
143 remaining time series. The resulting drydown time series (red circles) is shown in (d). Note that
144 gauge-based precipitation is only used for demonstrating the contrasting error statistics in parts
145 (a) to (c) and verification of the selected drydown time series (d). In-situ-based soil moisture (θ)
146 from Agricultural Research Service (ARS) Little Washita (Oklahoma, $34^\circ 35' \text{N}$, $97^\circ 53' \text{W}$) during
147 the 2016 June-July-August months is used here for demonstration.

148

149 2.2 Soil loss function determination

150 2.2.1 Soil loss function parameter optimization

151 The overall strategy for $L(\theta)$ identification is to fit each of the six possible forms shown in
152 Figure 1b to 1g to the observed soil moisture losses on pixel-by-pixel bases. Either cross
153 validation (Akbar et al. 2018) or information criteria can be used to avoid over-fitting. The
154 infrequent sampling of locally-rare environmental states, however, can weaken the power of
155 cross-validation of $L(\theta)$ models. We therefore directly analyze $L(\theta)$ based on all available
156 drydown data using the small-sample biased-corrected Akaike information criterion (AICc,
157 Burnham and Anderson (2004)) to perform parsimonious model selection.

158 Taking the most complex ABC form of $L(\theta)$ for illustration, the loss function can be
 159 expressed as:

$$y_A = \alpha_1(\theta - \theta_w), \quad \text{if } \theta < \theta_* \quad (3)$$

$$y_B = c, \quad \text{if } \theta_* \leq \theta < \theta_{fc} \quad (4)$$

$$y_C = \alpha_2(\theta - \theta_{fc}) + c, \quad \text{if } \theta \geq \theta_{fc} \quad (5)$$

160 where y_A , y_B and y_C are the estimated $d\theta/dt$ for the three different phases of $L(\theta)$ – see
 161 Figure 1; α_1 and α_2 are the slopes for Stage-II ET and drainage, respectively; and c is a
 162 constant estimated as $\alpha_1(\theta_* - \theta_w)$ by setting $\theta = \theta_*$ in (3). As with Akbar et al. (2018), the
 163 possible $L(\theta)$ forms in Figure 1 reflect the general landscape soil moisture state impact on
 164 hydrologic fluxes. However, a constant, low-rate, stage III evaporation regime (when $\theta < \theta_w$) is
 165 not included in this study. This is because the stage III evaporation rate is generally lower than
 166 0.005 (for arid to semi-arid regions) and 0.01 $\text{m}^3/(\text{m}^3 \text{ day})$ (for semi-humid and humid regions) –
 167 see Figure 9 of Sehgal et al. (2021b). These rates are much lower than the retrieval error of
 168 SMAP and hence, this evaporation stage is not considered in this study.

169 For a given combination of θ_w , θ_* , θ_{fc} , the slope parameters (i.e., α_1 and α_2) can be
 170 explicitly determined via linear regression. In effect, we first optimize only three (i.e., θ_w , θ_* ,
 171 θ_{fc}), instead all five parameters with SMCS. By reducing the dimensionality of the estimation
 172 problem, it is more robust to parameter equifinality and local optima problems (Dong et al.
 173 2015; Dong et al. 2016; Moradkhani et al. 2005).

174 At first, SMCS is initialized with n particles (i.e., parameter combinations, $\theta^j = [\theta_w^j, \theta_*^j, \theta_{fc}^j]$,
 175 with j ranging from 1 to n) randomly drawn from the entire parameter space. For each θ^j ,
 176 $L(\theta)$ can be estimated using linear regression – see (3) to (5). The fitting error for this particle is
 177 calculated as the quadratic mis-fit:

$$e^j = \sum (y - y_{obs})^2 \quad (6)$$

178 where y and y_{obs} are estimated and observed $d\theta/dt$, respectively. Based on e^j , the likelihood

179 (l) of θ_j can be quantified as:

$$l_j = \frac{1}{(2\pi\sigma^2)^{m/2}} \exp\left(-0.5 \frac{e^j}{\sigma^2}\right). \quad (7)$$

180 Where σ is the standard deviation of the observation error, m is the number of observations.
181 As shown in [Dong et al. \(2015\)](#), σ is essentially a parameter controlling the convergence speed
182 of SMCS. The likelihood is positively correlated to the accuracy of θ_j , irrespective to the choice
183 of σ . However, extremely low σ values may lead to severe particle degeneracy problems
184 ([Dong et al. 2016](#)). Based on these considerations, a default value of $0.02 \text{ m}^3/(\text{m}^3 \text{ day})$ is used
185 for σ and if the maximal likelihood of the particles is lower than 10^{-99} , σ will be set to 0.2
186 $\text{m}^3/(\text{m}^3 \text{ day})$ to prevent particle degeneracy.

187 Based on the likelihood function, the normalized importance weight (denoted as w_j) of
188 each particle is calculated as:

$$w_j = l_j / \sum l_j. \quad (8)$$

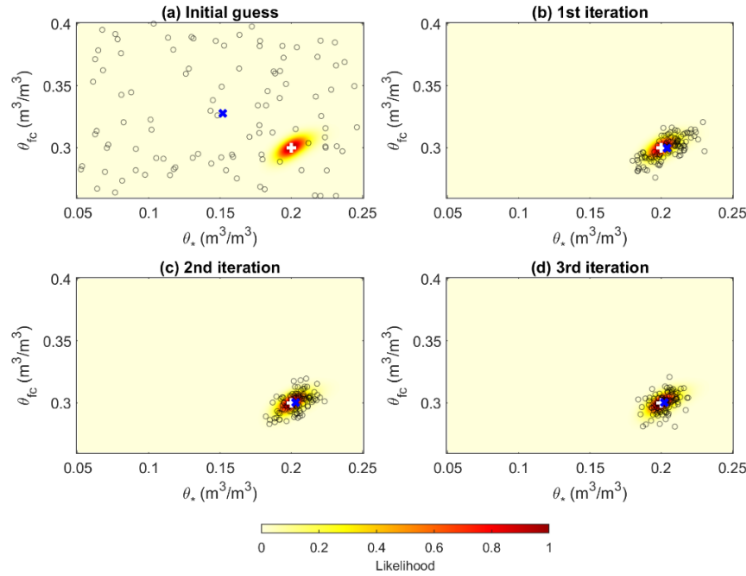
189 The particles are then resampled to discard particles with low importance weights (at a
190 probability of $1 - w_j$), using the procedure shown in [Smith and Gelfand \(1992\)](#). After
191 resampling, each particle is perturbed to enhance the sampling power of the parameter
192 posterior:

$$\theta_j = \beta \theta_j + (1 - \beta) \theta_k + \varepsilon \quad (9)$$

193 where β is a temporal constant and ε is white noise. Given the most complicated class-ABC
194 form of $L(\theta)$ only has three free parameters, our algorithm is generally insensitive to the
195 choice of β and ε . Therefore, $\beta = 0.95$ and ε with standard deviation of 5% of the
196 posterior distribution are used in this study.

197 Figure 3 provides an illustrative example of the SMCS optimization. We start by initializing
198 the SMCS with particles randomly drawn from the entire parameter space (Figure 3a). Based on
199 the importance weights of each particle (calculated using (8)), inaccurate particles are discarded
200 by resampling, and the resulting particles are randomly perturbed using (9) – leading to

201 significantly improved (likelihood) parameter posteriors (Figure 3b). By repeating the above
 202 processes, the mean of the particles gradually converges to the true parameters (Figure 3c and
 203 d).



204
 205 **Figure 3.** An illustrative example of the SMCS parameter optimization procedure using 100
 206 particles (grey open circles). Parts (a) to (d) show the evolution of particles after each iteration
 207 (or resampling). The synthetic “truth” is generated using the class-ABC form of $L(\theta)$ with
 208 pre-defined parameters (white plus sign). Each gray open circle represents the parameter
 209 combinations of a particle and the mean of all particles is denoted as the blue cross. For
 210 simplicity, only θ_* and θ_{fc} are shown here for demonstration.

211
 212 *2.2.2 Soil moisture loss functional form determination*

213 The SMCS algorithm is applied for all the six candidate forms of $L(\theta)$ (see Figure 1). Based
 214 on the optimized parameters (i.e., θ_w , θ_* , θ_{fc}), AICc is used to compare the performance of
 215 different $L(\theta)$ forms, i.e., model selection. For each $L(\theta)$ form, AICc is calculated as:

$$AICc = N \ln \left(\frac{e}{N} \right) + 2K + \frac{2K^2 + 2K}{n - K - 1} \quad (10)$$

216 where K is the number of parameters of the $L(\theta)$, N is the number of observations, and e is
 217 the fitting error of a specific $L(\theta)$ form based on SMCS optimized parameter, which is
 218 calculated analogously using (6) (Burnham and Anderson 2004).

219 To further enhance model selection, physical and statistical constraints are also applied. For
220 example, θ should not limit evaporation when it is above $0.40 \text{ m}^3/\text{m}^3$ and hence, class-A has to
221 be rejected – given the field capacity of clay is approximately $0.37 \text{ m}^3/\text{m}^3$ (Zhang and Schaap
222 2017). Therefore, in addition to AICc, we also include physical and statistical constraints in the
223 loss function determination: i) if the maximum θ value exceeds $0.40 \text{ m}^3/\text{m}^3$, class-A is rejected;
224 ii) if θ_* is lower than the 5th percentile of the θ time series, class-AB and ABC are rejected; iii)
225 if θ_{fc} is higher than the 95th percentile of the θ time series, class-BC is rejected; iv) if the
226 drainage slope (α_2) is smaller than the slope of stage-II evaporation (α_1), class-ABC is rejected.
227 Although four physical constrains are implemented, $L(\theta)$ is mainly determined by AICc. These
228 constraints are typically triggered at locations with strong dry-wet transitions and relatively
229 poor data quality.

230 Synthetic experiments demonstrate that the two-stage strategy is robust to variations in
231 sample size and observation errors. In addition, synthetic tests show that 300 particles are
232 sufficient to provide satisfactory results, with 100% $L(\theta)$ classification accuracy and
233 $R^2 > 0.95$ for low observation error scenarios, and with some reduced accuracy for increased
234 observation error levels (Figure S1). The detailed synthetic experiment design and results are
235 shown in Section 1 of the Supporting Information.

236 *2.3 Quantification of evaporation water availability and hydrologic tipping points*

237 We use soil moisture thresholds estimated from Section 2.2 to estimate the evaporation
238 water availability index (denoted as Π):

$$\Pi = \min\left(1, \frac{\theta - \theta_w}{\theta_* - \theta_w}\right). \quad (11)$$

239 This Π metric has traditionally been used in physically-based hydrological models (Mintz
240 and Walker 1993) and remote sensing evaporation retrievals (Martens et al. 2017) to evaluate
241 evaporation water stress. It is worth noting that Π is insensitive to multiplicative and additive
242 soil moisture retrieval biases – see demonstrations in Section 2 of the Supporting Information –
243 which makes it particularly suitable for our analysis, given the remote sensing soil moisture
244 biases are relatively unknown at the global scale (Dong et al. 2020a).

245 Based on Π , we seek to highlight regions influenced by both evaporation regimes, or those
246 at land surface tipping points. Over these regions, climate change/variability is more likely to
247 cause evaporation regime transitions. Therefore, this metric should leverage the time of a
248 landscape spent in both Stage-I and II evaporation regimes. Here, we propose a tipping point
249 metric (Φ) which is calculated as:

$$\Phi = 1 - |2\text{Prob}(\Pi < 1) - 1| \quad (12)$$

250 As shown in equation (12), humid regions constantly dominated by Stage-II ET (i.e., Π is
251 constantly 1, leading to $\text{Prob}(\Pi < 1) = 0$) have a Φ value of 0 – meaning no transitions in
252 evaporation regimes. Likewise, arid regions with Π constantly lower than 1 will also have
253 $\Phi = 0$. In contrast, Φ will approach 1 over dry-wet transitional climate zones, which
254 experience frequent transitions in Stage-I and II ET regimes. For instance, regions with 50% of
255 $\Pi < 1$ and 50% of $\Pi = 1$ will have the maximum Φ value of 1.

256 Note that regions with $\Phi \approx 0$ are not insensitive to hydroclimatic variability or change. For
257 example, evaporation strongly depends on the variability of precipitation and atmospheric
258 evaporative demand in arid regions (Feldman et al. 2022; Short Gianotti et al. 2020), but such
259 responses are mostly linear (see Figure 1b). In contrast, areas with high Φ values tend to
260 present nonlinear transitions between evaporation regimes, which may lead to abruptly
261 increased hydroclimate extremes (Zhang et al. 2020), once soil moisture drops below θ_* .
262 Additionally, Φ reflects multi-year evaporation regime statistics, which may not be applicable
263 to short time scale analyses. Finally, Φ closer to 1 indicates a higher likelihood of transitions,
264 but does not directly indicate frequent transitioning across the critical soil moisture threshold.

265 2.4 Data

266 Surface soil moisture estimates from the NASA Soil Moisture Active Passive (SMAP) mission
267 are used to quantify the global soil moisture drydown patterns (O'Neill et al. 2020). The global
268 level-3 36-km SMAP data from 1 April 2015 to 1 April 2021 are acquired from the National Snow
269 and Ice Data Center archive (Entekhabi et al. 2010). SMAP data collected from 6 AM overpasses
270 and based on the single channel algorithm are used in this study (Entekhabi et al. 2014).
271 Retrievals affected by snow, ice, frozen ground, complex topography, or high vegetation density

272 (vegetation water contented higher than 7kg/m^2) are excluded. Note that SMAP is mostly
273 sensitive to the top 5 cm surface soil moisture conditions (Njoku and Entekhabi 1996). However,
274 our recent study demonstrates that surface and deeper rootzone soil moisture are consistent in
275 identifying evaporation regime transitions (Dong et al. 2022a). The soil moisture retrieval error
276 impacts on our estimates are comprehensively discussed in Sections 1 and 2 of the Supporting
277 Information. The number of valid SMAP observation after drydown identification is shown in
278 Figure S2.

279 In some tests and analyses, we use flux tower observations of daily latent heat (LE) and
280 sensible heat (H) fluxes collected from the AmeriFlux network (Novick et al. 2018). Land surface
281 energy partitioning is quantified based on the commonly used evaporation fraction, or $EF =$
282 $LE/(LE + H)$. These EF observations are used to evaluate the effectiveness of SMAP-based
283 drydown analysis in quantifying the land surface energy partition. Only sites with at least 5
284 years of available data during April 2015 to April 2021 are used. The spatial distribution of the
285 resulting 37 flux tower observations is shown in Figure S3.

286 Finally, the aridity index (AI, calculated as the ratio of precipitation and potential ET) is used
287 to evaluate microclimate influence on hydrological regime transition frequencies. The global
288 and daily 0.1-degree precipitation data from Multi-Source Weighted-Ensemble Precipitation
289 (Beck et al. 2019) and the 0.25-degree and daily potential evaporation estimates from the
290 Global Land Evaporation Amsterdam Model (Martens et al. 2017) are used to define pixel-wise
291 AI values. Both products are resampled onto 36-km SMAP grids through bilinear interpolation.

292

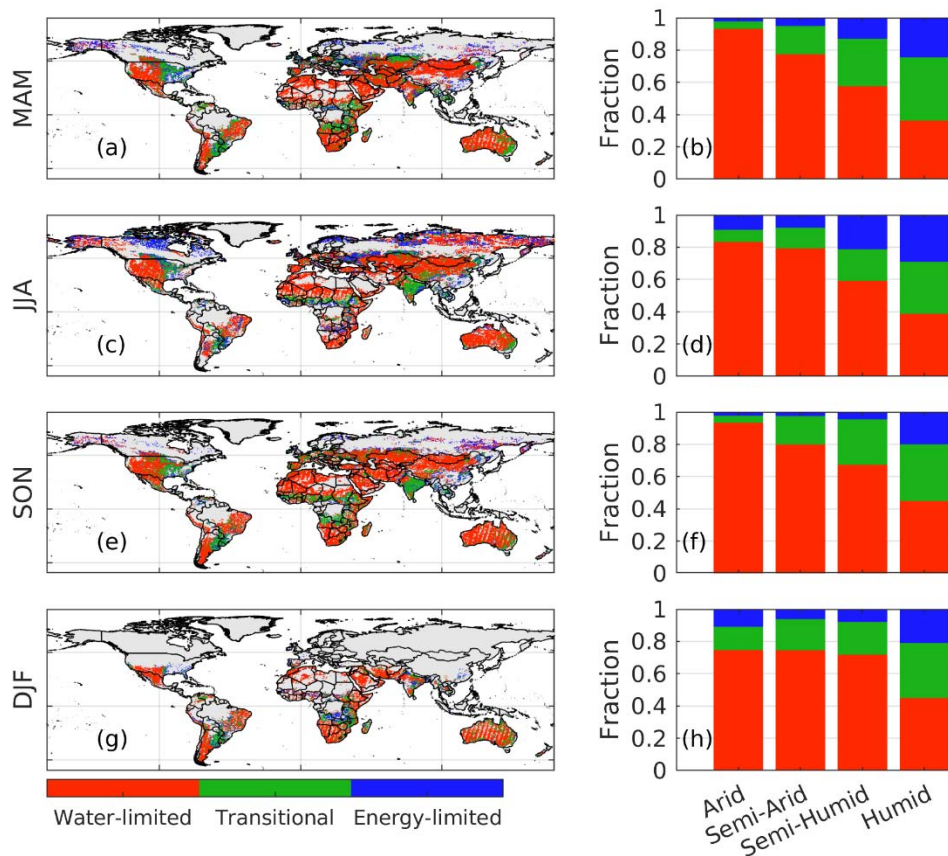
293 **3 Results and Discussions**

294 *3.1 Influence of climate and seasons on the distribution of evaporation regimes*

295 Loss function $L(\theta)$ forms are estimated using the framework described in Section 2. Using
296 the SMAP soil moisture product alone, the global land regions are categorized into
297 water-limited (class-A), transitional (class-AB and ABC) and energy-limited (class-B, BC and D)
298 evaporation regimes, according to their soil moisture thresholds (i.e., θ_w , θ_* and θ_{fc} , see

299 Figure 1). Note that these thresholds may be affected by both climate and vegetation phenology
 300 – making them potentially seasonally variable (Haghighi et al. 2018). Hence, we perform our
 301 analysis separately for each season (Figure 4).

302 As expected, arid and semi-arid regions are dominated by water-limited regimes, e.g., such
 303 as in the western US, the North Africa, central Asia and central Australia (Figure 4a). These
 304 findings are qualitatively confirmed by Figure 4b, which shows that more than 90% of land
 305 pixels within arid regions display water-limited evaporation regimes.



306

307 **Figure 4.** Global distribution of evaporation regimes for different seasons (first column) and the
 308 fraction of each regime for different climate zones (second column). Arid, semi-arid, sub-humid
 309 and humid regions are corresponding to pixels with AI values of 0 - 0.2, 0.2 - 0.5, 0.5 - 0.65 and >
 310 0.65, respectively. Water-limited cases are pixels constantly dominated by Class-A $L(\theta)$, while
 311 energy-limited regimes are pixels with the absence of Class-A $L(\theta)$. Transitional ET regimes are
 312 cases containing both stage-I and stage-II evaporation, e.g., Class-AB and -ABC $L(\theta)$.

313

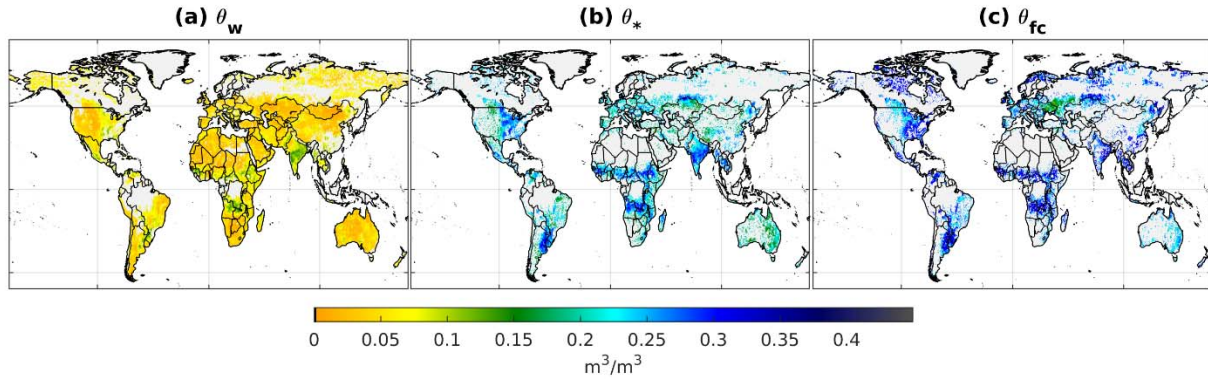
314 A significant fraction of land pixels within arid and semi-arid regions shows transitional or
315 energy-limited evaporation regimes. This situation applies for approximately 2% of land pixels
316 within the arid region. This is particularly noticeable in India during DJF, in response to
317 large-scale winter irrigation (Douglas et al. 2006). Relative to arid regions, the portion of
318 transitional regimes substantially increases in semi-arid and semi-humid regions (Figure 4b, d
319 and f). Fluctuations of dry and wet conditions within these climate regions lead to more
320 frequent switching between evaporation regimes. Likewise, energy-limited regimes are
321 primarily shown in humid areas – suggesting the overall water supply (i.e., P) exceeds the
322 evaporative demand. Overall, the seasonal transitions of hydrological regimes shown in Figure 4
323 are mainly due to seasonal variability in microclimate and human activities.

324

325 *3.2 Factors influencing soil moisture thresholds*

326 In our parameter estimation, all pixel-wise soil moisture thresholds are estimated separately
327 for each season. However, seasonal variations in soil moisture thresholds are usually small. We
328 acknowledge that soils with clay content higher than 50% may exhibit stronger seasonal
329 variability in soil moisture thresholds (Sehgal et al. 2021b). However, such cases are only
330 applicable for less than 1% of global land grids, according to SMAP soil texture map, which is
331 derived based on multiple commonly used global soil texture datasets. Because of this low
332 temporal variability, we only focus on the seasonal mean of these soil moisture thresholds for
333 the remainder of this study.

334 Seasonally averaged soil moisture thresholds, θ_w , θ_* , and θ_{fc} are shown in Figure 5.
335 While Monte Carlo or bootstrapping based uncertainty analysis of Figure 5 is computationally
336 expensive, synthetic experiments on a case with error statistics comparable to SMAP
337 observations demonstrate that the coefficient of determination of soil moisture threshold
338 estimates is above 0.84 (see Figure S1). In addition, Figure 5 is consistent with those derived
339 based on independent methods (Akbar et al. 2018; Sehgal et al. 2021b). These results suggest
340 the general robustness of our parameter estimates in Figure 5.



341

342 **Figure 5.** Global distribution of all-season-mean θ_w (a), θ_* (b) and θ_{fc} (c). Gray shadings
 343 represent land areas that soil moisture drydown analysis cannot be performed or the soil
 344 moisture thresholds cannot be estimated using the corresponding $L(\theta)$.

345

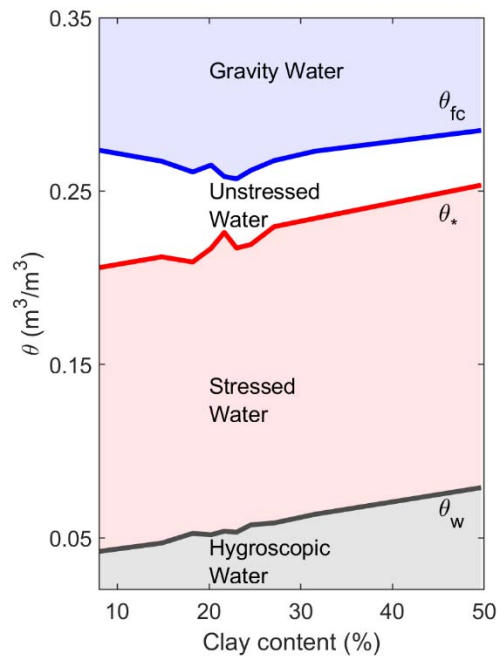
346 The soil moisture thresholds that distinguish different hydrologic regimes are themselves a
 347 function of vegetation characteristics and soil hydraulic properties and hence, persistent
 348 geographic patterns of these variables are expected. As evident in Figure 5, the thresholds
 349 demonstrate strong dependency on the dominant climate zones. For example, θ_* in the
 350 semi-humid central US (lightly vegetated) is approximately $0.15 \text{ m}^3/\text{m}^3$ and sharply increases to
 351 $0.3 \text{ m}^3/\text{m}^3$ in the humid eastern US (densely vegetated, Figure 2b). Such strong
 352 climate-vegetation-soil links are expected, given climate is a major determinant of vegetation
 353 and the vegetation rooting system that can also significantly affect the soil hydraulic properties
 354 (Hao et al. 2019). Furthermore, θ_* is dependent on the process of roots extracting water from
 355 the unsaturated soil matrix and there it will depend on vegetation traits, soil hydraulic
 356 properties, lower atmosphere winds, and potential evaporative demand (Feldman et al. 2019;
 357 Haghghi et al. 2018). These findings are qualitatively confirmed by Figure S4, and are also
 358 consistent with previous soil moisture drydown analysis (Akbar et al. 2018; Sehgal et al. 2021a,
 359 b).

360 In addition to climate and vegetation dependencies, soil hydraulic properties are also known
 361 to be a strong function of soil texture (Zhang and Schaap 2017), which defines vegetation and
 362 evaporation water availability (Kramer and Boyer 1983). Figure 6 further shows SMAP-based soil

363 moisture thresholds as a function of clay content. This depiction of soil moisture thresholds as a
364 function of soil texture appears as a conceptual diagram in many hydrology textbooks, based on
365 laboratory hydraulic test data (Kramer and Boyer 1983). Here we use the global SMAP soil
366 moisture product to re-visit this classic diagram but based on global and landscape scale data.
367 We show that θ_* and θ_w demonstrate a strong increasing trend with increased clay content.
368 However, a slightly more complicated θ_{fc} and clay content relationship is evident in Figure 6,
369 which may be related to limited sample size of some soil classes, e.g., limited number of pixels
370 with sandy soils are available for a robust detection of the drainage process. Additionally, SMAP
371 overpass intervals are 2 to 3 days which is longer than typical drainage time to field capacity
372 after rainstorms. Therefore, the drainage hydrologic regime is more difficult to capture from
373 remote sensing data. Nevertheless, our thresholds as a function of clay content largely reflect
374 that of known soil hydraulic diagrams.

375 We note that samples within each clay class of Figure 6 may contain significant variability in
376 vegetation and microclimate conditions, as well as sub-grid heterogeneity of land surface
377 conditions. Therefore, Figure 6 is aimed at linking the landscape-scale soil texture impacts to soil
378 moisture thresholds, and is not directly comparable to classic laboratory-based sample
379 conditions.

380 Figure 6 also provides direct insights into evaporation water availability (denoted as Π). The
381 soil water component above θ_{fc} (blue shaded area) percolates quickly to deep sub-layers,
382 which is less likely to be used by evaporation or vegetation. In contrast, soil water potential is
383 too negative to be effectively used for evaporation when soil moisture drops below θ_w .
384 Evaporation water supply is bracketed by soil moisture dynamics when it is between θ_{fc} and
385 θ_w . This storage can be further divided as un-stressed and stressed water according to θ_*
386 (white and red shadings). This figure directly illustrates the physical link of Π (calculated using
387 (11)) and evaporation water viability. Specifically, $\Pi = 1$ means that soil moisture content is
388 above θ_* and evaporation is not limited by soil moisture – see the white and blue shadings in
389 Figure 6. In contrast, $\Pi < 1$ suggests that soil moisture availability starts to become a limiting
390 factor of evaporation (see the red shadings in Figure 6).



391

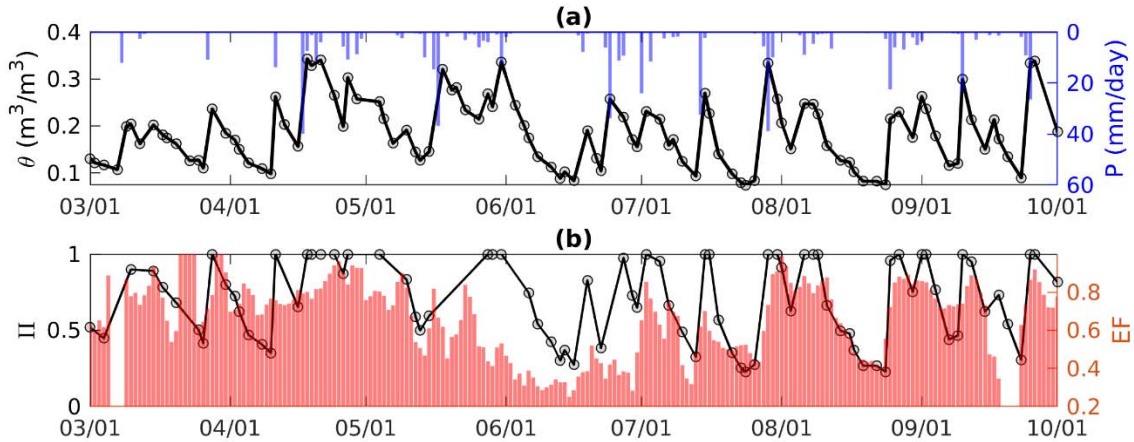
392 **Figure 6.** Soil water conditions as a function of clay content. Solid lines are averaged soil
 393 moisture thresholds sampled across different clay contents based on Figure 5.

394

395 *3.3 SMAP-based Evaporation water availability and land-surface energy partition*

396 The metric Π can be estimated on a pixel-by-pixel basis using SMAP-based soil moisture
 397 thresholds (again using seasonally-averaged values of the soil moisture thresholds). The Π time
 398 series at the US-ARM site (Raz-Yaseef et al. 2015) in Oklahoma is shown in Figure 7 for
 399 demonstration.

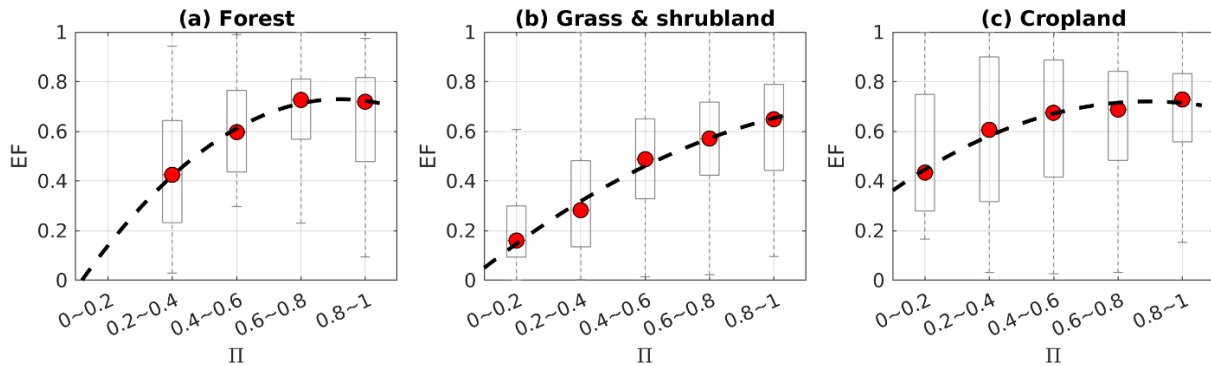
400 The consistency between the SMAP-based Π and flux tower-based EF temporal dynamics is
 401 evident in Figure 7b, which is particularly noticeable in JJA months (warm season). For example,
 402 a consistent decrease of Π is observed in the middle of August, leading to a similar reduction
 403 in EF. The water stress is alleviated by precipitation events in late August (Figure 7a). As a result,
 404 the US-ARM site shifts to energy-limited regimes, as Π approaches 1, which yields sharply
 405 increased EF (Figure 7b).



406

407 **Figure 7.** Evaluation of Π at US-ARM site located in Oklahoma (36.6N^o, 97.4^oW). (a):
 408 MSWEP-based P and SMAP observed soil moisture time series during March to September 2016.
 409 (b): Flux tower observed EF and SMAP-based Π during the period. The red bars are US-ARM
 410 observed EF and black line is the SMAP-based Π .

411



412

413 **Figure 8.** EF as a function of Π sampled from AmeriFlux sites under different land cover types.
 414 Estimates from all seasons are used, with 1, 23 and 13 sites available for forest, grass and
 415 shrubland, and cropland, respectively. The box and the whiskers represent the interquartile and
 416 5th – 95th percentile range of EF values, respectively, which are sampled across all the available
 417 sites. The red circle is the median EF value of each bin.

418

419 A more comprehensive evaluation of Π is shown in Figure 8, which samples the
 420 SMAP-based Π and flux tower observed EF relationship from different land cover types. Note
 421 that EF is affected by multitude factors, e.g., microclimate, land cover, soil properties,
 422 observation error, etc. These factors may all inflate the interquartile ranges of the EF values
 423 presented in Figure 8. Nonetheless, for all three land cover types, EF is a monotonically

424 increasing function of Π . It is also noticeable that EF is relatively more sensitive to Π at dry
425 conditions, and this sensitivity decreases with increased Π . These findings are consistent with
426 previous modeled (Dirmeyer et al. 2000; Lu et al. 2016) and observation-based (Short Gianotti
427 et al. 2019a) EF and soil water availability relationships.

428 *3.4 Frequency of evaporation regime transition at the global scale*

429 Based on Π , we estimate the frequency of global evaporation regime changes using the Φ
430 metric – see (12) for metric definition. The spatial distribution of Φ shows regions of the global
431 land surface that can potentially experience water and energy balance regime changes as a
432 result of climate variability and change. They span the central US, Europe, the Pampas region in
433 South America, Sahel in Africa, the Indian subcontinent and the east coast of Australia (Figure 9).
434 Geographically, they cover vast regions that separate persistently water-limited areas (arid and
435 hyperarid areas) and forested humid areas. In addition, it is noteworthy that Φ tends to
436 increase in the summer and autumn, i.e., JJA and SON for Northern Hemisphere, and MAM and
437 DJF for the Southern Hemisphere – see boxplots in Figure 9. These months represent a temporal
438 transition between evaporation and vegetation phenological regimes in many land regions of
439 the globe. Thus, these regions regularly switch between regimes, and climate variability or
440 change can prolong or contract the evaporation regime dominance from one season to the
441 next.

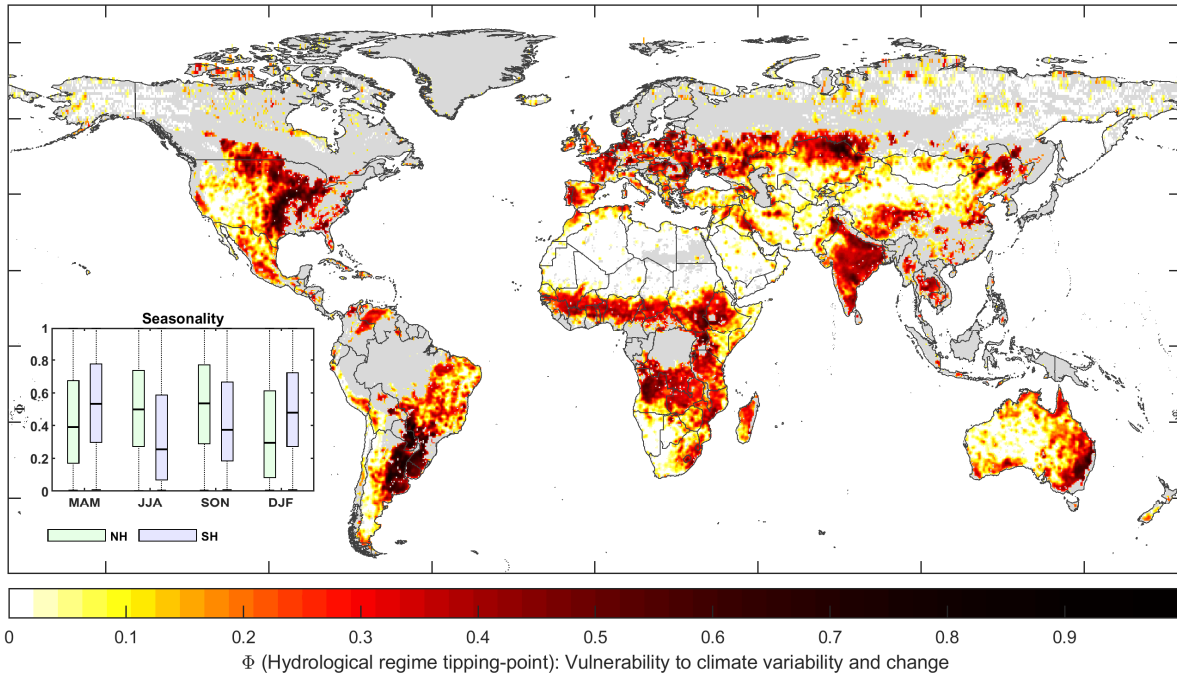
442 These findings add an observation-driven perspective to previous global classification of
443 land-atmosphere coupling strength based on models (Dirmeyer 2011; Koster et al. 2004;
444 Mueller and Seneviratne 2012; Seneviratne et al. 2006). The strength of the coupling between
445 local water and energy balances affects how closely the surface moisture state and the
446 near-surface air temperature are linked. In turn, this reflects how influential the land surface
447 dynamics are on the evolution of the near-surface atmosphere and ultimately, land-atmosphere
448 coupling.

449 Importantly, Φ seasonality and global distributions in Figure 9 are entirely
450 observation-based which means that they are not affected by process parameterizations in
451 models. Thus, they can be used to assess models and guide model development.

452 We recognize that extreme regional climate change and land use change may have significant
453 impacts on soil moisture thresholds and by extension, the global distribution of Φ . This may

454 lead to a different vulnerability map as that shown in Figure 9. For such cases, Φ estimates
455 should be sampled during the period that is representative of these environmental changes.

456



457
458 **Figure 9.** The global and annual mean distribution of land regions at the tipping-point between
459 water-limited and energy-limited evaporation regimes. The metric Φ captures how vulnerable
460 the landscape is to climate variability and change. Given unit shifts in soil moisture, regions with
461 Φ approaching one will experience the most change in how their surface water and energy are
462 coupled. Seasonal variations of Φ over the Northern (NH) and Southern Hemisphere (SH) are
463 shown in the inset boxplots. The metric is based on satellite observations only. The transitional
464 conditions between the evaporation regimes are at their peak during the summer and autumn
465 seasons (i.e., JJA and SON for NH, and DJF and MAM for SH) and span large areas in the
466 semi-arid to semi-humid landscapes.

467

468

469 4. Conclusion

470 Land evaporation switches between energy- and water-limited regimes that signify the
471 coupling and decoupling of water, energy and carbon cycles across landscape. The transition
472 point is dependent on environmental factors, the primary one being the soil moisture state
473 variable. Therefore, regions that are characterized by soil moisture distributions closer to this
474 soil moisture threshold, i.e., with frequent energy- to water-limited evaporation regime
475 transitions, are likely to be more vulnerable to climate variability and change. However, such

476 nonlinear evaporation regime transitions are typically identified using model-based approaches,
477 which is subject to model-specific assumptions and errors.

478 In this study, we use multi-year SMAP surface soil moisture observations to identify the
479 frequency of landscape changes between energy- and water-limited regimes. We first identify
480 soil moisture drydown time series. Then we estimate the soil moisture threshold value that
481 delineates the transitions between evaporation regimes. Based on this framework, an
482 observation-based index of evaporation water availability (Π) is developed and assessed using
483 37 flux-tower sites across the CONUS. As determined by θ_* , Π is expected to be influenced by
484 multiple factors, such as microclimate, vegetation cover and soil properties (Figure S4). A key
485 advantage of our approach is that it implicitly integrates all the environmental information and
486 provide large-scale estimates of evaporation regime transitions in a data-driven manner.

487 Based on the Π estimates, we further define an index of land surface vulnerability to
488 climate variability and change (the index Φ). Conceptually, the Φ index quantifies the
489 frequency of evaporation regime changes, which is associated with transitions from or to
490 coupled versus uncoupled land surface water and energy balance. This in turn affects the
491 sensitivity of the lower atmosphere to soil moisture changes, which has direct implications for
492 investigating the onset and the development of hydroclimate extremes, e.g., heatwaves and
493 flash droughts. The new tipping-point metric is based only on observations which allows it to be
494 used to assess land surface components of Earth System models. The observation-based metric
495 also adds to the suites of existing (mostly model-based) metrics for identifying critical regions
496 for land-atmosphere coupling.

497 Finally, we would like to note that global Φ distribution in Figure 9 is sampled over a
498 6-year period, which may not reflect the impact of historical long-term microclimate trends,
499 abrupt land use changes and climate cycles like El Niño-Southern Oscillation (ENSO). However,
500 except for extreme cases, the six years of soil moisture observations are generally
501 representative of long-term landscape wetness climatology (Dong et al. 2020a). Nonetheless,
502 applying our analysis on long-term European Space Agency Climate Change Initiative (ESA CCI)
503 soil moisture product (Dorigo et al. 2017) may provide insights into long-term global Φ
504 variations. However, ESA CCI soil moisture uses sensors with temporally varied soil moisture
505 error and sampling depth, and algorithms that can isolate these impacts are required.

506 **Acknowledgement**

507 Jianzhi Dong is funded by National Natural Science Foundation of China (52179021). The
508 authors with MIT affiliation acknowledge funding from NASA in the form of a sponsored
509 research grant (Subcontract No. 1510842). Andrew F. Feldman was supported by an
510 appointment to the NASA Postdoctoral Program at the NASA Goddard Space Flight Center,
511 administered by Oak Ridge Associated Universities under contract with NASA.

512 **Data Statement**

513 The SMAP data are acquired from <https://smap.jpl.nasa.gov/data/>. MSWEP and GLEAM data
514 are accessible at <http://www.gloh2o.org/mswep/> and <https://www.gleam.eu/>, respectively.

515 Codes for the drydown analysis is available at:
516 <https://github.com/dongjianzhi/Soil-moisture-drydown-analysis>

517 **Reference**

518 Akbar, R., Gianotti, D.J.S., McColl, K.A., Haghghi, E., Salvucci, G.D., & Entekhabi, D. (2018).
519 Estimation of landscape soil water losses from satellite observations of soil moisture. *Journal of*
520 *Hydrometeorology*, 19, 871-889

521 Bateni, S.M., Entekhabi, D., Margulis, S., Castelli, F., & Kergoat, L. (2014). Coupled estimation of
522 surface heat fluxes and vegetation dynamics from remotely sensed land surface temperature
523 and fraction of photosynthetically active radiation. *Water Resources Research*, 50, 8420-8440

524 Beck, H.E., Wood, E.F., Pan, M., Fisher, C.K., Miralles, D.G., Van Dijk, A.I.J.M., McVicar, T.R., &
525 Adler, R.F. (2019). MSWEP V2 global 3-hourly 0.1 precipitation: methodology and quantitative
526 assessment. *Bulletin of the American Meteorological Society*, 100, 473-500

527 Berg, A., & Sheffield, J. (2018). Soil moisture–evapotranspiration coupling in CMIP5 models:
528 relationship with simulated climate and projections. *Journal of Climate*, 31, 4865-4878

529 Biederman, J.A., Scott, R.L., Arnone Iii, J.A., Jasoni, R.L., Litvak, M.E., Moreo, M.T., Papuga, S.A.,
530 Ponce-Campos, G.E., Schreiner-McGraw, A.P., & Vivoni, E.R. (2018). Shrubland carbon sink
531 depends upon winter water availability in the warm deserts of North America. *Agricultural and*
532 *Forest Meteorology*, 249, 407-419

533 Buitink, J., Swank, A.M., van der Ploeg, M., Smith, N.E., Benninga, H.-J.F., van der Bolt, F.,
534 Carranza, C.D.U., Koren, G., van der Velde, R., & Teuling, A.J. (2020). Anatomy of the 2018
535 agricultural drought in The Netherlands using in situ soil moisture and satellite vegetation
536 indices. *Hydrology and Earth System Sciences*, 24, 6021-6031

537 Burnham, K.P., & Anderson, D.R. (2004). Multimodel inference: understanding AIC and BIC in
538 model selection. *Sociological methods & research*, 33, 261-304

539 Crow, W.T., Chen, F., Reichle, R.H., & Xia, Y. (2019). Diagnosing Bias in Modeled Soil
540 Moisture/Runoff Coefficient Correlation Using the SMAP Level 4 Soil Moisture Product. *Water*
541 *Resources Research*, 55, 7010-7026

542 Crow, W.T., Gomez, C.A., Sabater, J.M., Holmes, T., Hain, C.R., Lei, F., Dong, J., Alfieri, J.G., &
543 Anderson, M.C. (2020). Soil Moisture–Evapotranspiration Overcoupling and L-Band Brightness
544 Temperature Assimilation: Sources and Forecast Implications. *Journal of Hydrometeorology*, 21,
545 2359-2374

546 Crow, W.T., Huffman, G.J., Bindlish, R., & Jackson, T.J. (2009). Improving satellite-based rainfall
547 accumulation estimates using spaceborne surface soil moisture retrievals. *Journal of*
548 *Hydrometeorology*, 10, 199-212

549 Crow, W.T., Lei, F., Hain, C., Anderson, M.C., Scott, R.L., Billesbach, D., & Arkebauer, T. (2015).
550 Robust estimates of soil moisture and latent heat flux coupling strength obtained from triple
551 collocation. *Geophysical Research Letters*, 42, 8415-8423

552 Denissen, J.M.C., Teuling, A.J., Reichstein, M., & Orth, R. (2020). Critical soil moisture derived
553 from satellite observations over Europe. *Journal of Geophysical Research: Atmospheres*, 125,
554 e2019JD031672

555 Dirmeyer, P.A. (2011). The terrestrial segment of soil moisture–climate coupling. *Geophysical*
556 *Research Letters*, 38

557 Dirmeyer, P.A., Balsamo, G., Blyth, E.M., Morrison, R., & Cooper, H.M. (2021). Land-atmosphere
558 interactions exacerbated the drought and heatwave over northern Europe during summer 2018.
559 *AGU Advances*, 2, e2020AV000283

560 Dirmeyer, P.A., Chen, L., Wu, J., Shin, C.-S., Huang, B., Cash, B.A., Bosilovich, M.G., Mahanama, S.,
561 Koster, R.D., & Santanello, J.A. (2018). Verification of land–atmosphere coupling in forecast
562 models, reanalyses, and land surface models using flux site observations. *Journal of*
563 *Hydrometeorology*, 19, 375-392

564 Dirmeyer, P.A., Zeng, F.J., Ducharne, A., Morrill, J.C., & Koster, R.D. (2000). The sensitivity of
565 surface fluxes to soil water content in three land surface schemes. *Journal of Hydrometeorology*,
566 1, 121-134

567 Dong, J., Akbar, R., Short Gianotti, D.J., Feldman, A.F., Crow, W.T., & Entekhabi, D. (2022a). Can
568 Surface Soil Moisture Information Identify Evapotranspiration Regime Transitions? *Geophysical*
569 *Research Letters*, 49, e2021GL097697

570 Dong, J., & Crow, W.T. (2018). The added value of assimilating remotely sensed soil moisture for
571 estimating summertime soil moisture-air temperature coupling strength. *Water Resources*
572 *Research*, 54, 6072-6084

573 Dong, J., Crow, W.T., Tobin, K.J., Cosh, M.H., Bosch, D.D., Starks, P.J., Seyfried, M., & Collins, C.H.
574 (2020a). Comparison of microwave remote sensing and land surface modeling for surface soil
575 moisture climatology estimation. *Remote Sensing of Environment*, 242, 111756

576 Dong, J., Dirmeyer, P.A., Lei, F., Anderson, M.C., Holmes, T.R.H., Hain, C., & Crow, W.T. (2020b).
577 Soil evaporation stress determines soil moisture-evapotranspiration coupling strength in land
578 surface modeling. *Geophysical Research Letters*, *47*, e2020GL090391

579 Dong, J., Lei, F., & Crow, W.T. (2022b). Land transpiration-evaporation partitioning errors
580 responsible for modeled summertime warm bias in the central United States. *Nature*
581 *communications*, *13*, 1-8

582 Dong, J., Steele-Dunne, S.C., Judge, J., & van de Giesen, N. (2015). A particle batch smoother for
583 soil moisture estimation using soil temperature observations. *Advances in Water Resources*, *83*,
584 111-122

585 Dong, J., Steele-Dunne, S.C., Ochsner, T.E., Hatch, C.E., Sayde, C., Selker, J., Tyler, S., Cosh, M.H.,
586 & van de Giesen, N. (2016). Mapping high-resolution soil moisture and properties using
587 distributed temperature sensing data and an adaptive particle batch smoother. *Water Resources*
588 *Research*, *52*, 7690-7710

589 Dorigo, W., Wagner, W., Albergel, C., Albrecht, F., Balsamo, G., Brocca, L., Chung, D., Ertl, M.,
590 Forkel, M., & Gruber, A. (2017). ESA CCI Soil Moisture for improved Earth system understanding:
591 State-of-the art and future directions. *Remote Sensing of Environment*, *203*, 185-215

592 Douglas, E.M., Niyogi, D., Frohling, S., Yeluripati, J.B., Pielke Sr, R.A., Niyogi, N., Vörösmarty, C.J.,
593 & Mohanty, U.C. (2006). Changes in moisture and energy fluxes due to agricultural land use and
594 irrigation in the Indian Monsoon Belt. *Geophysical Research Letters*, *33*

595 Entekhabi, D., Njoku, E.G., O'Neill, P.E., Kellogg, K.H., Crow, W.T., Edelstein, W.N., Entin, J.K.,
596 Goodman, S.D., Jackson, T.J., & Johnson, J. (2010). The soil moisture active passive (SMAP)
597 mission. *Proceedings of the IEEE*, *98*, 704-716

598 Entekhabi, D., Rodriguez-Iturbe, I., & Castelli, F. (1996). Mutual interaction of soil moisture state
599 and atmospheric processes. *Journal of Hydrology*, *184*, 3-17

600 Entekhabi, D., Yueh, S., & De Lannoy, G. (2014). SMAP handbook

601 Feldman, A.F., Short Gianotti, D.J., Trigo, I.F., Salvucci, G.D., & Entekhabi, D. (2019). Satellite-
602 based assessment of land surface energy partitioning–soil moisture relationships and effects of
603 confounding variables. *Water Resources Research*, *55*, 10657-10677

604 Feldman, A.F., Short Gianotti, D.J., Trigo, I.F., Salvucci, G.D., & Entekhabi, D. (2020). Land-
605 atmosphere drivers of landscape-scale plant water content loss. *Geophysical Research Letters*,
606 *47*, e2020GL090331

607 Feldman, A.F., Short Gianotti, D.J., Trigo, I.F., Salvucci, G.D., & Entekhabi, D. (2022). Observed
608 Landscape Responsiveness to Climate Forcing, *58*, e2021WR030316

609 Gallego-Elvira, B., Taylor, C.M., Harris, P.P., Ghent, D., Veal, K.L., & Folwell, S.S. (2016). Global
610 observational diagnosis of soil moisture control on the land surface energy balance. *Geophysical*
611 *Research Letters*, *43*, 2623-2631

612 Greve, P., Gudmundsson, L., Orłowsky, B., & Seneviratne, S.I. (2015). Introducing a probabilistic
613 Budyko framework. *Geophysical Research Letters*, *42*, 2261-2269

614 Haghighi, E., Short Gianotti, D.J., Akbar, R., Salvucci, G.D., & Entekhabi, D. (2018). Soil and

615 Atmospheric Controls on the Land Surface Energy Balance: A Generalized Framework for
616 Distinguishing Moisture-Limited and Energy-Limited Evaporation Regimes. *Water Resources*
617 *Research*, 54, 1831-1851

618 Hain, C.R., Mecikalski, J.R., & Anderson, M.C. (2009). Retrieval of an available water-based soil
619 moisture proxy from thermal infrared remote sensing. Part I: Methodology and validation.
620 *Journal of Hydrometeorology*, 10, 665-683

621 Hao, M., Zhang, J., Meng, M., Chen, H.Y.H., Guo, X., Liu, S., & Ye, L. (2019). Impacts of changes in
622 vegetation on saturated hydraulic conductivity of soil in subtropical forests. *Scientific reports*, 9,
623 1-9

624 Holmes, T.R.H., Hain, C.R., Crow, W.T., Anderson, M.C., & Kustas, W.P. (2018). Microwave
625 implementation of two-source energy balance approach for estimating evapotranspiration.
626 *Hydrology and Earth System Sciences*, 22, 1351-1369

627 Humphrey, V., Berg, A., Ciais, P., Gentine, P., Jung, M., Reichstein, M., Seneviratne, S.I., &
628 Frankenberg, C. (2021). Soil moisture-atmosphere feedback dominates land carbon uptake
629 variability. *Nature*, 592, 65-69

630 Jeremiah, E., Sisson, S.A., Sharma, A., & Marshall, L. (2012). Efficient hydrological model
631 parameter optimization with Sequential Monte Carlo sampling. *Environmental Modelling &*
632 *Software*, 38, 283-295

633 Koster, R.D., Dirmeyer, P.A., Guo, Z., Bonan, G., Chan, E., Cox, P., Gordon, C.T., Kanae, S.,
634 Kowalczyk, E., & Lawrence, D. (2004). Regions of strong coupling between soil moisture and
635 precipitation. *Science*, 305, 1138-1140

636 Kramer, P.J., & Boyer, J.S. (1983). *Water relations of plants and soils*. Academic press

637 Lei, F., Crow, W.T., Holmes, T.R.H., Hain, C., & Anderson, M.C. (2018). Global investigation of soil
638 moisture and latent heat flux coupling strength. *Water Resources Research*, 54, 8196-8215

639 Lorenz, R., Argüeso, D., Donat, M.G., Pitman, A.J., van den Hurk, B., Berg, A., Lawrence, D.M.,
640 Chéruy, F., Ducharne, A., & Hagemann, S. (2016). Influence of land-atmosphere feedbacks on
641 temperature and precipitation extremes in the GLACE-CMIP5 ensemble. *Journal of Geophysical*
642 *Research: Atmospheres*, 121, 607-623

643 Lu, Y., Dong, J., Steele-Dunne, S.C., & van de Giesen, N. (2016). Estimating surface turbulent heat
644 fluxes from land surface temperature and soil moisture observations using the particle batch
645 smoother. *Water Resources Research*, 52, 9086-9108

646 Martens, B., Miralles, D.G., Lievens, H., van der Schalie, R., de Jeu, R.A.M., Fernández-Prieto, D.,
647 Beck, H.E., Dorigo, W.A., & Verhoest, N.E.C. (2017). GLEAM v3: satellite-based land evaporation
648 and root-zone soil moisture. *Geoscientific Model Development*, 10, 1903-1925

649 Mintz, Y., & Walker, G.K. (1993). Global fields of soil moisture and land surface
650 evapotranspiration derived from observed precipitation and surface air temperature. *Journal of*
651 *Applied Meteorology and Climatology*, 32, 1305-1334

652 Miralles, D.G., Gentine, P., Seneviratne, S.I., & Teuling, A.J. (2019). Land-atmospheric feedbacks
653 during droughts and heatwaves: state of the science and current challenges. *Ann N Y Acad Sci*,

654 1436, 19-35

655 Miralles, D.G., Van Den Berg, M.J., Teuling, A.J., & De Jeu, R.A.M. (2012). Soil moisture-
656 temperature coupling: A multiscale observational analysis. *Geophysical Research Letters*, 39

657 Moradkhani, H., Hsu, K.L., Gupta, H., & Sorooshian, S. (2005). Uncertainty assessment of
658 hydrologic model states and parameters: Sequential data assimilation using the particle filter.
659 *Water Resources Research*, 41

660 Mueller, B., & Seneviratne, S.I. (2012). Hot days induced by precipitation deficits at the global
661 scale. *Proceedings of the national academy of sciences*, 109, 12398-12403

662 Njoku, E.G., & Entekhabi, D. (1996). Passive microwave remote sensing of soil moisture. *Journal*
663 *of Hydrology*, 184, 101-129

664 Novick, K.A., Biederman, J.A., Desai, A.R., Litvak, M.E., Moore, D.J.P., Scott, R.L., & Torn, M.S.
665 (2018). The AmeriFlux network: A coalition of the willing. *Agricultural and Forest Meteorology*,
666 249, 444-456

667 O'Neill, P., Chan, S., Bindlish, R., Chaubell, M., Colliander, A., Chen, F., Dunbar, S., Jackson, T.,
668 Peng, J., & Cosh, M. (2020). Soil Moisture Active Passive (SMAP) Project: Calibration and
669 Validation for the L2/3_SM_P Version 7 and L2/3_SM_P_E Version 4 Data Products

670 Orth, R. (2021). When the land surface shifts gears. *AGU Advances*, 2, e2021AV000414

671 Qiu, J., Crow, W.T., Dong, J., & Nearing, G.S. (2020). Model representation of the coupling
672 between evapotranspiration and soil water content at different depths. *Hydrology and Earth*
673 *System Sciences*, 24, 581-594

674 Raz-Yaseef, N., Billesbach, D.P., Fischer, M.L., Biraud, S.C., Gunter, S.A., Bradford, J.A., & Torn,
675 M.S. (2015). Vulnerability of crops and native grasses to summer drying in the US Southern
676 Great Plains. *Agriculture, Ecosystems & Environment*, 213, 209-218

677 Santanello Jr, J.A., Lawston, P., Kumar, S., & Dennis, E. (2019). Understanding the impacts of soil
678 moisture initial conditions on NWP in the context of land-atmosphere coupling. *Journal of*
679 *Hydrometeorology*, 20, 793-819

680 Schwingshackl, C., Hirschi, M., & Seneviratne, S.I. (2017). Quantifying Spatiotemporal Variations
681 of Soil Moisture Control on Surface Energy Balance and Near-Surface Air Temperature. *Journal*
682 *of Climate*, 30, 7105-7124

683 Sehgal, V., Gaur, N., & Mohanty, B.P. (2021a). Global Flash Drought Monitoring using Surface Soil
684 Moisture. *Water Resources Research*, e2021WR029901

685 Sehgal, V., Gaur, N., & Mohanty, B.P. (2021b). Global surface soil moisture drydown patterns.
686 *Water Resources Research*, 57, e2020WR027588

687 Seneviratne, S.I., Corti, T., Davin, E.L., Hirschi, M., Jaeger, E.B., Lehner, I., Orlowsky, B., & Teuling,
688 A.J. (2010). Investigating soil moisture-climate interactions in a changing climate: A review.
689 *Earth-Science Reviews*, 99, 125-161

690 Seneviratne, S.I., Lüthi, D., Litschi, M., & Schär, C. (2006). Land-atmosphere coupling and
691 climate change in Europe. *Nature*, 443, 205-209

692 Seneviratne, S.I., Wilhelm, M., Stanelle, T., van den Hurk, B., Hagemann, S., Berg, A., Cheruy, F.,

693 Higgins, M.E., Meier, A., & Brovkin, V. (2013). Impact of soil moisture-climate feedbacks on
694 CMIP5 projections: First results from the GLACE-CMIP5 experiment. *Geophysical Research*
695 *Letters*, *40*, 5212-5217

696 Short Gianotti, D.J., Akbar, R., Feldman, A.F., Salvucci, G.D., & Entekhabi, D. (2020). Terrestrial
697 evaporation and moisture drainage in a warmer climate. *Geophysical Research Letters*, *47*,
698 e2019GL086498

699 Short Gianotti, D.J., Rigden, A.J., Salvucci, G.D., & Entekhabi, D. (2019a). Satellite and station
700 observations demonstrate water availability's effect on continental-scale evaporative and
701 photosynthetic land surface dynamics. *Water Resources Research*, *55*, 540-554

702 Short Gianotti, D.J., Salvucci, G.D., Akbar, R., McColl, K.A., Cuenca, R., & Entekhabi, D. (2019b).
703 Landscape Water Storage and Subsurface Correlation From Satellite Surface Soil Moisture and
704 Precipitation Observations. *Water Resources Research*, *55*, 9111-9132

705 Smith, A.F.M., & Gelfand, A.E. (1992). Bayesian statistics without tears: a sampling–resampling
706 perspective. *The American Statistician*, *46*, 84-88

707 Williams, I.N., & Torn, M.S. (2015). Vegetation controls on surface heat flux partitioning, and
708 land-atmosphere coupling. *Geophysical Research Letters*, *42*, 9416-9424

709 Zhang, P., Jeong, J.-H., Yoon, J.-H., Kim, H., Wang, S.Y.S., Linderholm, H.W., Fang, K., Wu, X., &
710 Chen, D. (2020). Abrupt shift to hotter and drier climate over inner East Asia beyond the tipping
711 point. *Science*, *370*, 1095-1099

712 Zhang, Y., & Schaap, M.G. (2017). Weighted recalibration of the Rosetta pedotransfer model
713 with improved estimates of hydraulic parameter distributions and summary statistics (Rosetta3).
714 *Journal of Hydrology*, *547*, 39-53

715 Zhou, S., Williams, A.P., Berg, A.M., Cook, B.I., Zhang, Y., Hagemann, S., Lorenz, R., Seneviratne,
716 S.I., & Gentine, P. (2019). Land-atmosphere feedbacks exacerbate concurrent soil drought and
717 atmospheric aridity. *Proc Natl Acad Sci U S A*, *116*, 18848-18853

718

Figure 1.

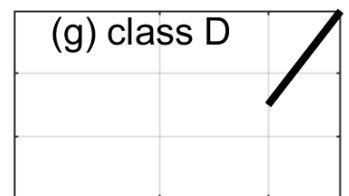
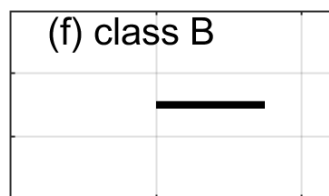
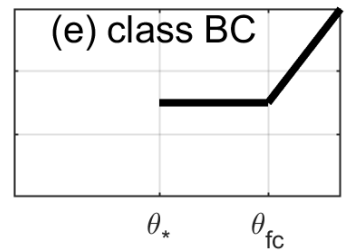
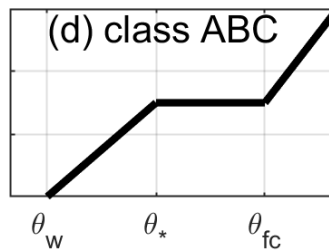
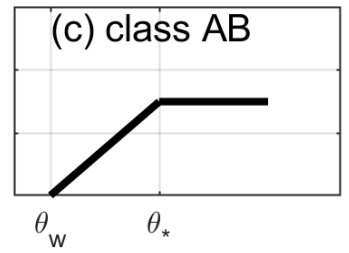
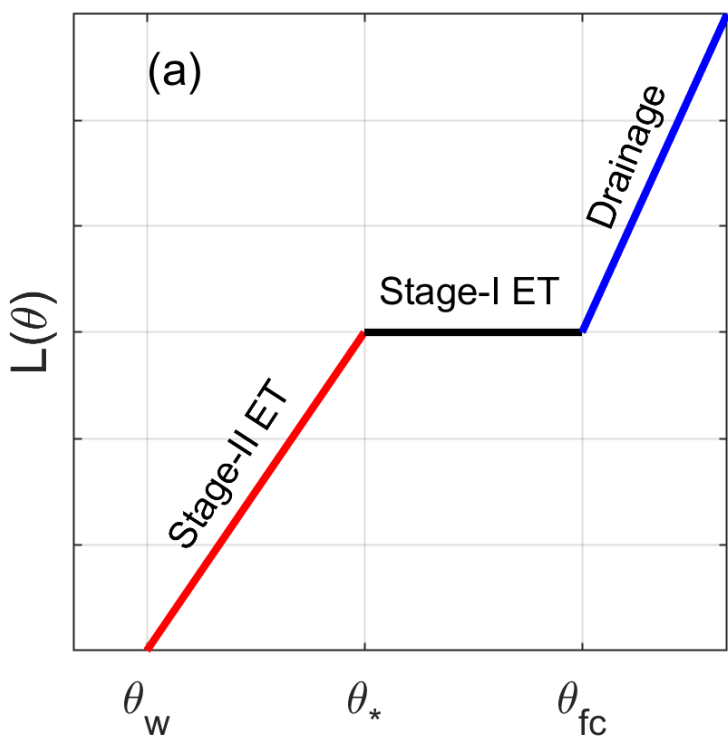


Figure 2.

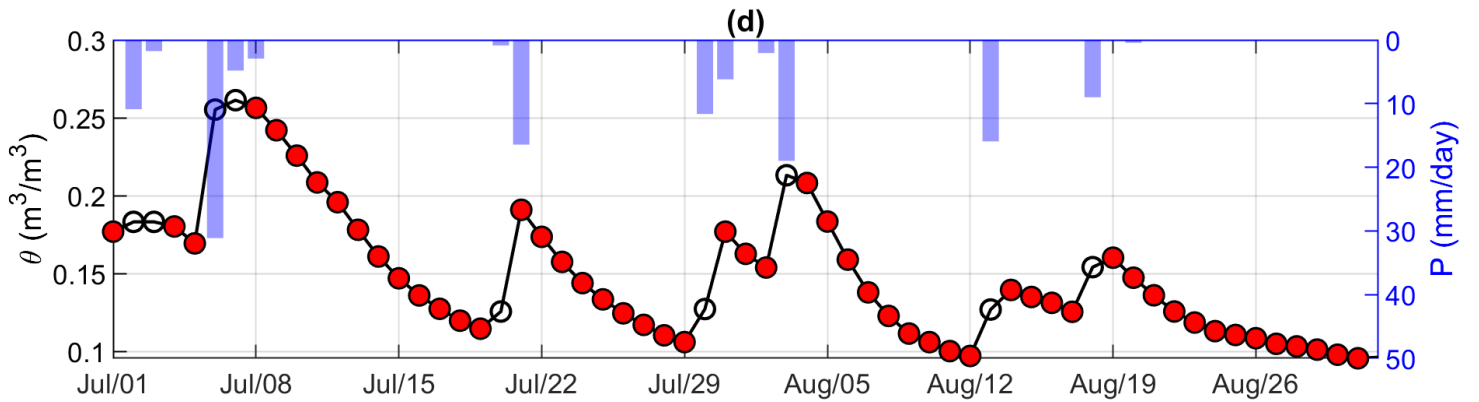
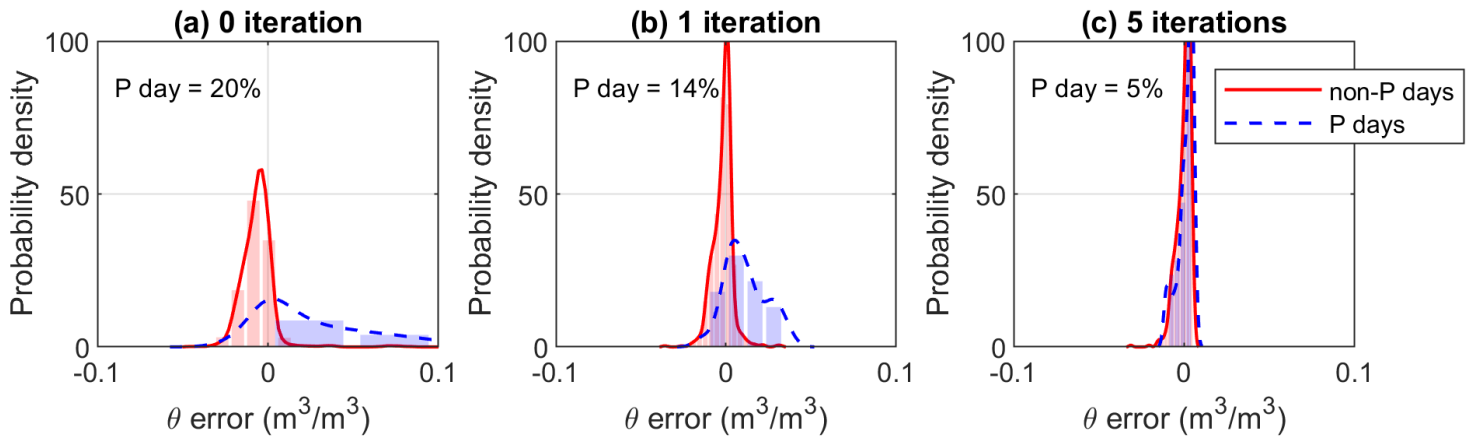


Figure 3.

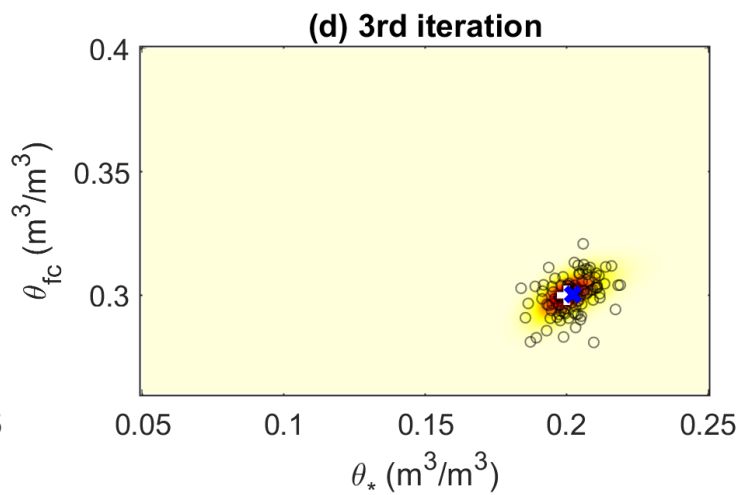
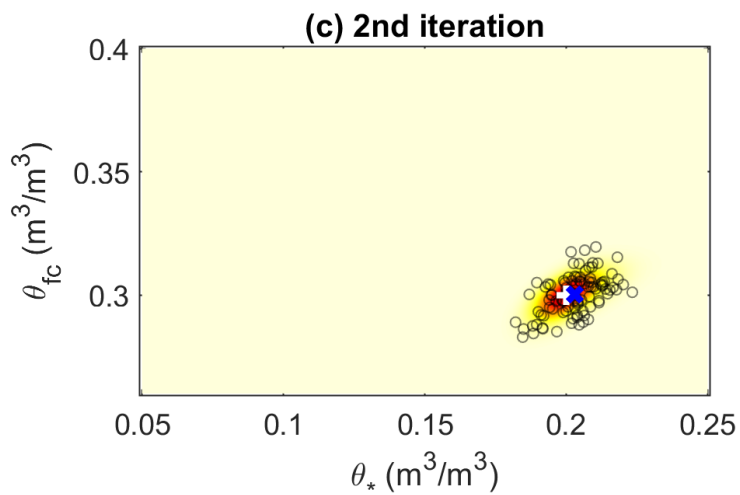
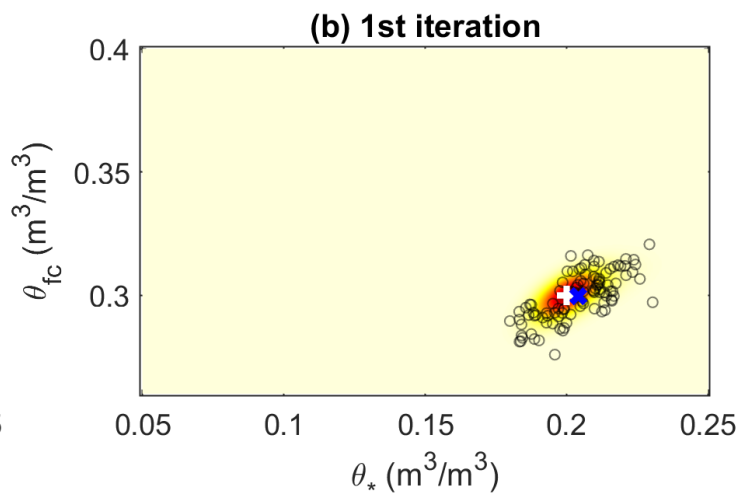
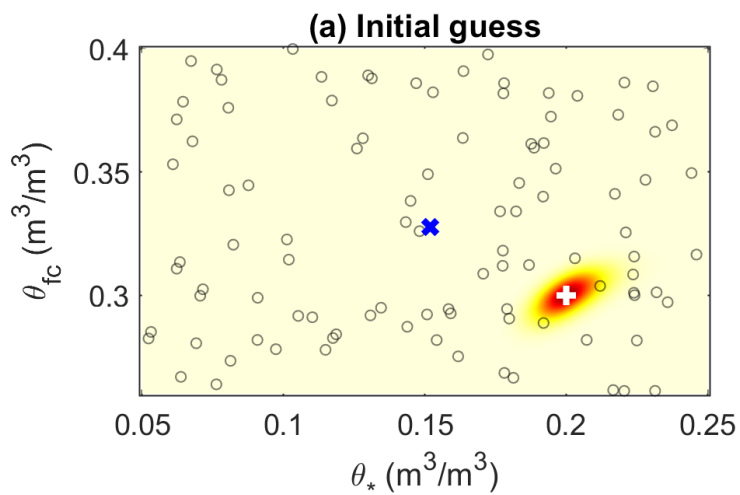
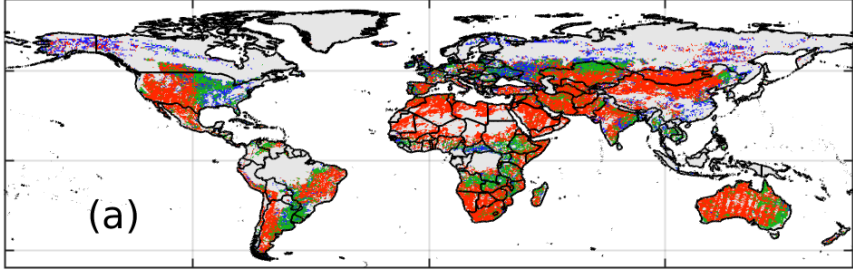
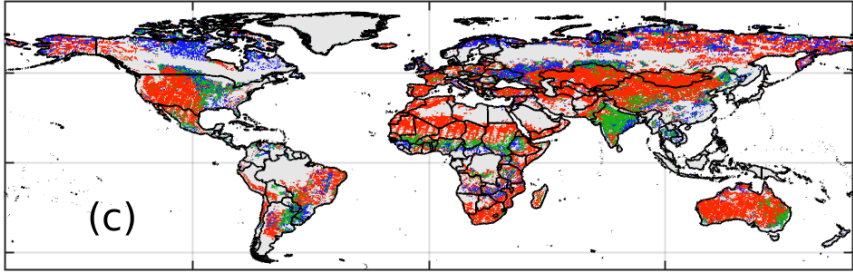


Figure 4.

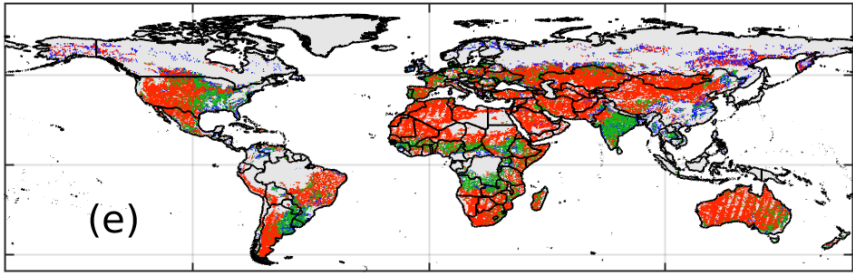
MAM



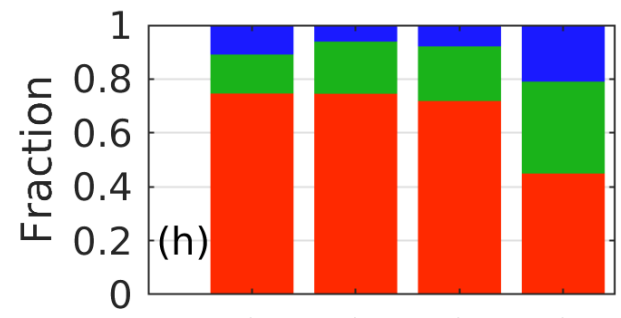
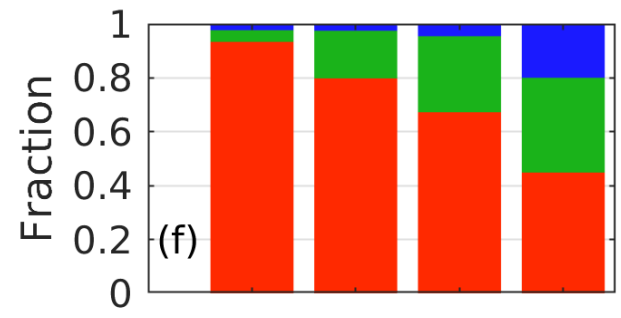
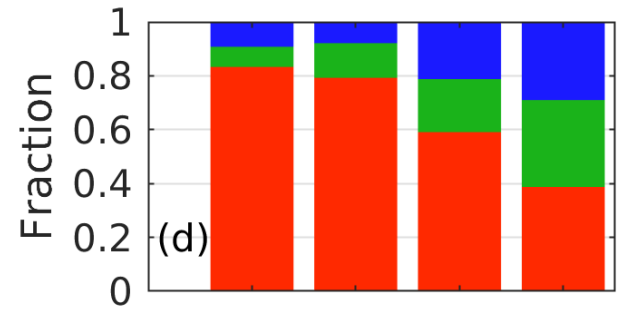
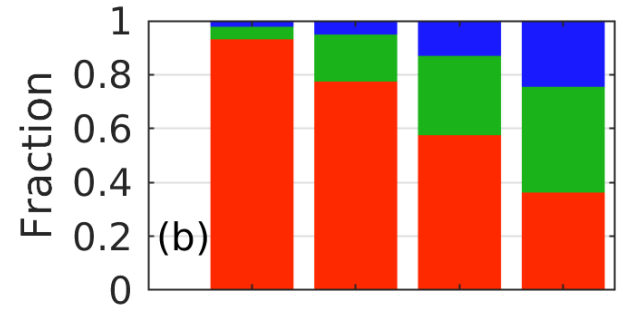
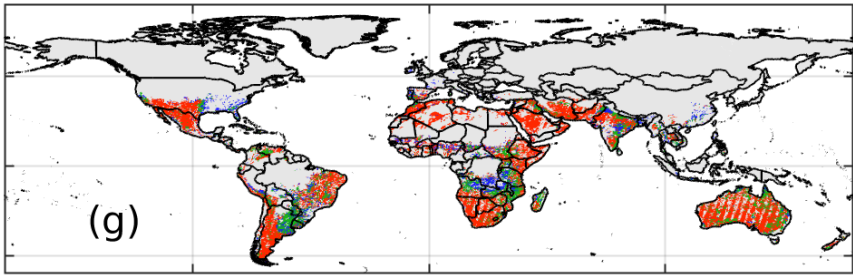
JJA



SON

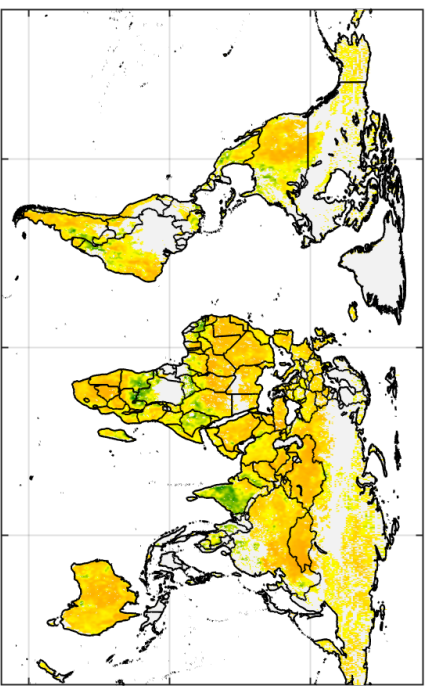


DJF

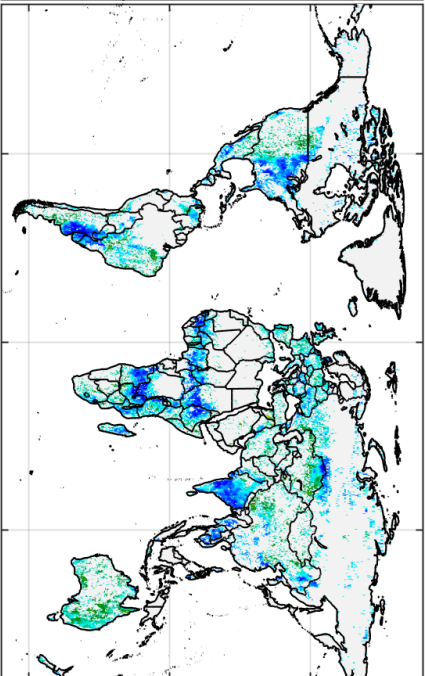


Arid
Semi-Arid
Semi-Humid
Humid

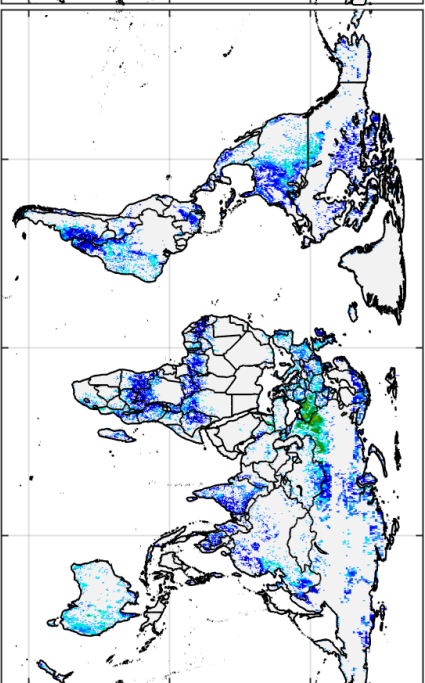
Figure 5.



(a) θ_w



(b) θ_*



(c) θ_{fc}

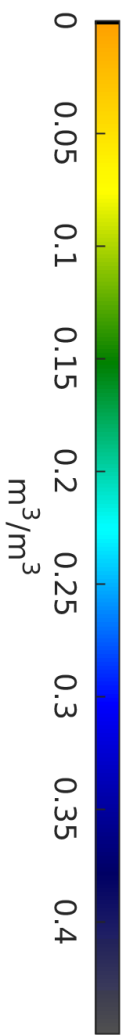


Figure 6.

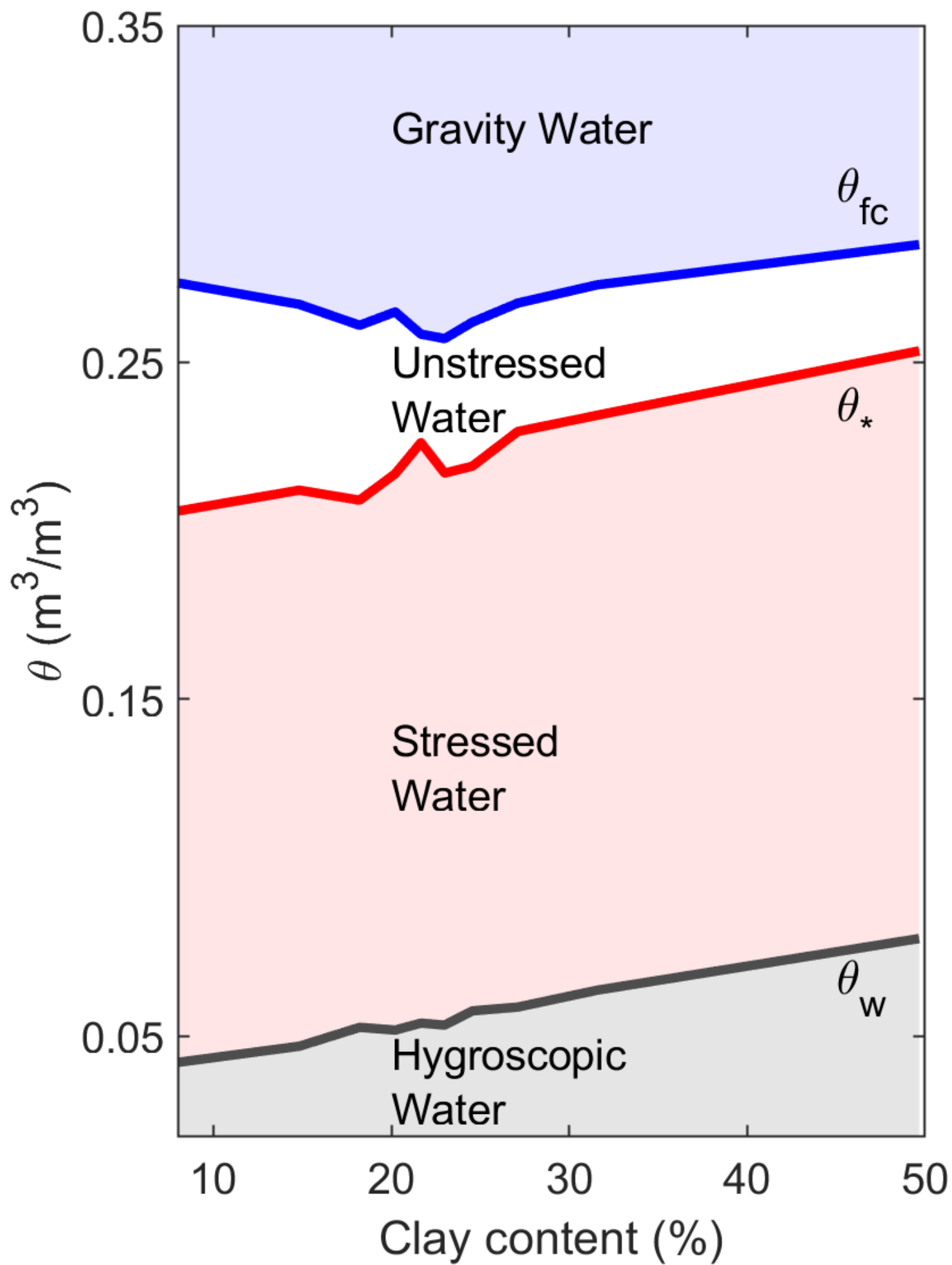


Figure 7.

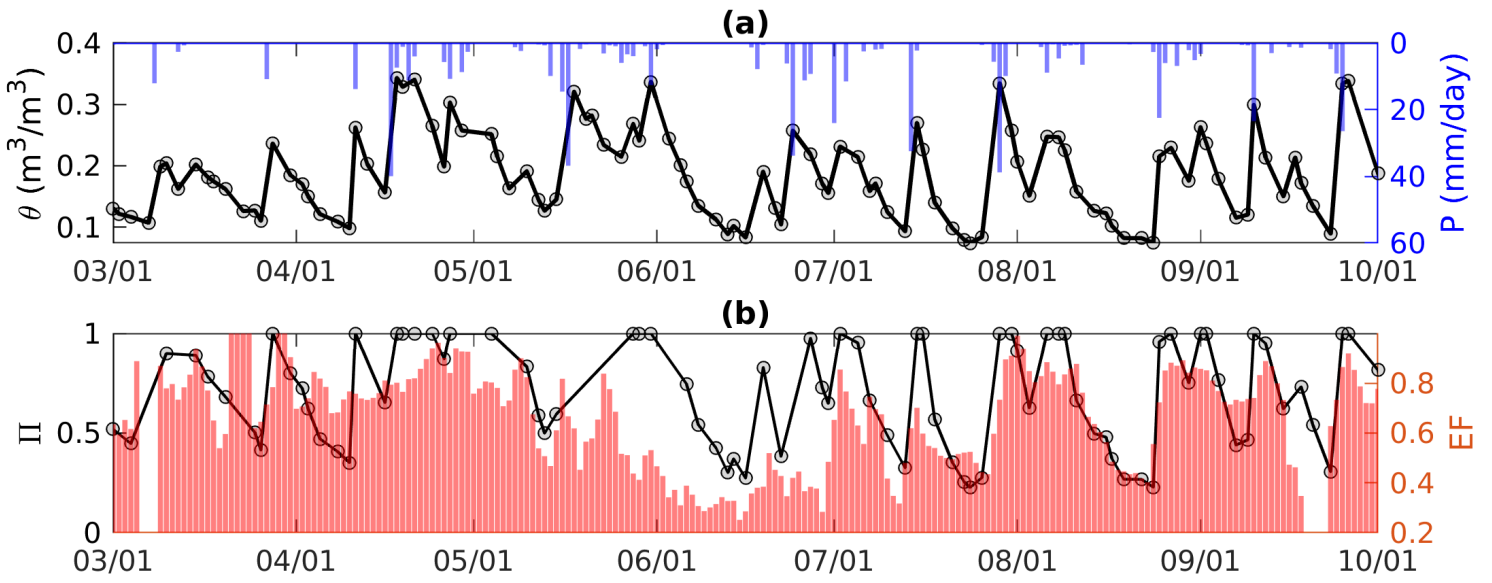


Figure 8.

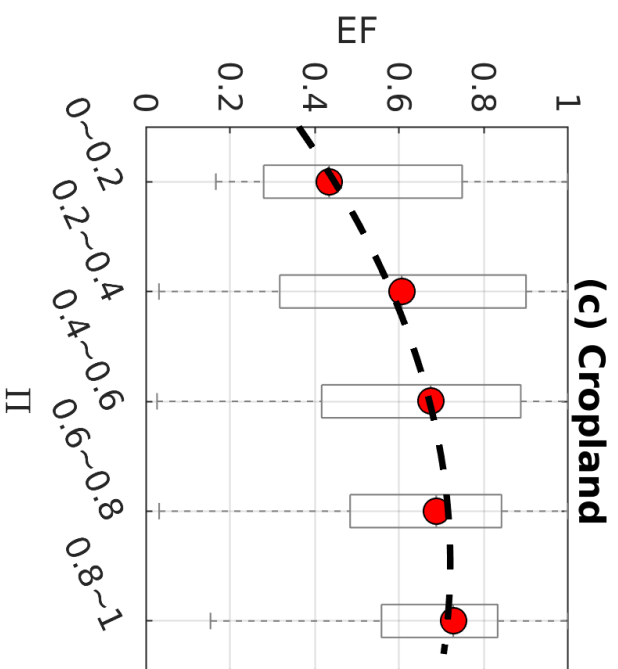
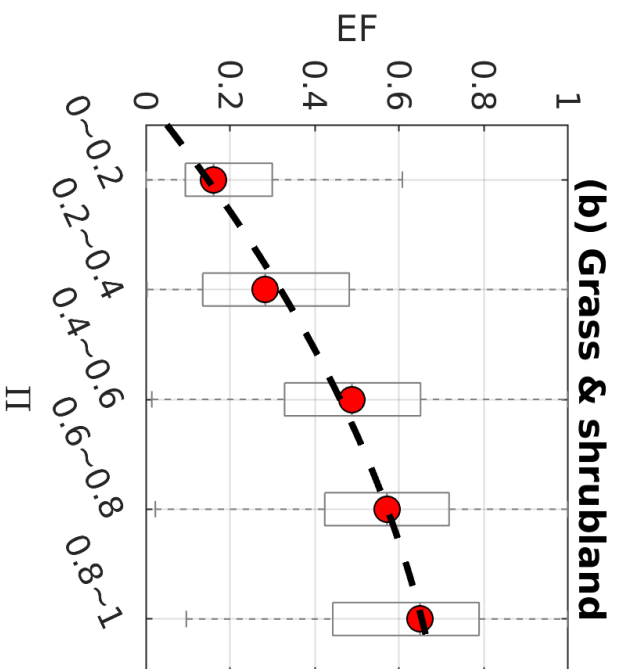
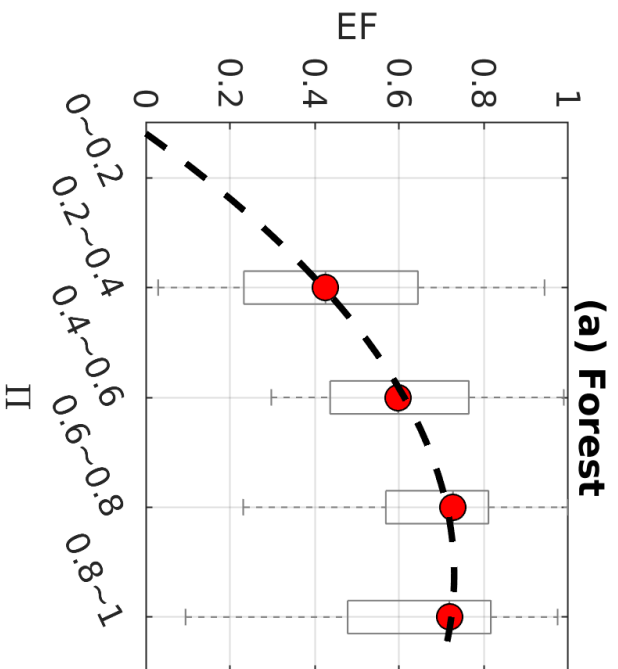


Figure 9.

